The Astrophysical Journal, 801:63 (19pp), 2015 March 1 doi:10.1088/0004-637X/801/1/63

ALMA MULTI-LINE IMAGING OF THE NEARBY STARBURST NGC 253

David S. Meier[1,10], Fabian Walter[2,10], Alberto D. Bolatto[3], Adam K. Leroy[4], Jürgen Ott[5], Erik Rosolowsky[6], Sylvain Veilleux[3,7], Steven R. Warren[3], Axel Weiß[8], Martin A. Zwaan[9], and Laura K. Zschaechner[2]
[1] New Mexico Institute of Mining and Technology, 801 Leroy Place, Socorro, NM 87801, USA; dmeier@nmt.edu
[2] Max-Planck Institut für Astronomie, Königstuhl 17, D-69117 Heidelberg, Germany
[3] Department of Astronomy and Joint Space-Science Institute, University of Maryland, College Park, MD 20742, USA
[4] National Radio Astronomy Observatory, 520 Edgemont Road, Charlottesville, VA 22903, USA
[5] National Radio Astronomy Observatory, Pete V. Domenici Array Science Center, P.O. Box O, Socorro, NM 87801, USA
[6] Department of Physics, University of Alberta, Edmonton, AB T6G 2E1, Canada
[7] Department of Astronomy, University of Maryland, College Park, MD 20742, USA
[8] Max Planck Institut für Radioastronomie, Auf dem Hügel 69, D-53121 Bonn, Germany
[9] European Southern Observatory, Karl-Schwarzschild-Str. 2, D-85748 Garching bei München, Germany
Received 2014 May 24; accepted 2015 January 7; published 2015 March 4

ABSTRACT

We present spatially resolved (∼50 pc) imaging of molecular gas species in the central kiloparsec of the nearby starburst galaxy NGC 253, based on observations taken with the Atacama Large Millimeter/submillimeter Array. A total of 50 molecular lines are detected over a 13 GHz bandwidth imaged in the 3 mm band. Unambiguous identifications are assigned for 27 lines. Based on the measured high $CO/C^{17}O$ isotopic line ratio ($\gtrsim$350), we show that ^{12}CO(1–0) has moderate optical depths. A comparison of the HCN and HCO^+ with their ^{13}C-substituted isotopologues shows that the HCN(1–0) and HCO^+(1–0) lines have optical depths at least comparable to CO(1–0). $H^{13}CN/H^{13}CO^+$ (and $H^{13}CN/HN^{13}C$) line ratios provide tighter constraints on dense gas properties in this starburst. SiO has elevated abundances across the nucleus. HNCO has the most distinctive morphology of all the bright lines, with its global luminosity dominated by the outer parts of the central region. The dramatic variation seen in the HNCO/SiO line ratio suggests that some of the chemical signatures of shocked gas are being erased in the presence of dominating central radiation fields (traced by C_2H and CN). High density molecular gas tracers (including HCN, HCO^+, and CN) are detected at the base of the molecular outflow. We also detect hydrogen β recombination lines that, like their α counterparts, show compact, centrally peaked morphologies, distinct from the molecular gas tracers. A number of sulfur based species are mapped (CS, SO, NS, C_2S, H_2CS, and CH_3SH) and have morphologies similar to SiO.

Key words: astrochemistry – galaxies: evolution – galaxies: formation – galaxies: individual (NGC 253) – radio lines: ISM

1. INTRODUCTION

Characterizing the physical properties of the molecular gas phase in galaxies, the key phase for star formation (review by Kennicutt & Evans 2012), is among the main drivers in the studies of nearby galaxies. The ^{12}CO line is by far the brightest millimeter–wave molecular line in the interstellar medium (ISM) and has therefore been the main tracer of the molecular medium in both low- and high-redshift studies (e.g., reviews by Bolatto et al. 2013b and Carilli & Walter 2013). Even though CO emission is a reasonable tracer of the morphology and mass associated with the molecular ISM, observations of other tracer molecules, that have different critical densities and excitation temperatures, provide key information to constrain the physical processes in the ISM. Studying a whole suite of molecular line tracers sheds light on the chemical state of the ISM, including the gas cooling and ionization balance in the molecular ISM. Ultimately, surveying provides the means by which to characterize molecular cloud conditions that are affected by the galactic environment, including feedback and shocks caused by star formation, and dynamical processes within a galaxy (e.g., Meier & Turner 2005).

Millimeter line surveys of nearby galaxies using single-dish telescopes have shown that their spectra are rich in molecular lines (e.g., Usero et al. 2004; Martín et al. 2006; Costagliola et al. 2011; Snell et al. 2011; Aladro et al. 2011, 2013). However, given the resolution of single-dish telescopes, most of these studies could only provide integrated measurements, making it difficult to investigate spatial changes in chemical properties. Spatially resolved surveys using millimeter interferometers have been limited to only a handful of transitions due to small bandwidths and low sensitivity (e.g., Meier & Turner 2005, 2012; Meier et al. 2014; Martín et al. 2015). These studies demonstrate the presence of strong chemical differentiation can exist within the molecular gas in nearby galaxies and their usefulness for constraining the evolutionary properties of the nucleus.

The newly commissioned Atacama Large Millimeter/submillimeter Array (ALMA) facility is revolutionizing chemical studies of galaxies. Its sensitivity, even in "Early Science" mode is unprecedented, and molecules that are typically significantly fainter than the brightest ones (i.e., CO, HCN, HCO^+, CN) can be detected in reasonable integration times. In addition ALMA's large instantaneous bandwidth of $\Delta\nu = 8$ GHz implies that multiple lines (in particular in the 3 mm band where $\Delta\nu/\nu$ is highest) are covered in each observation. *The study presented here does not intend to discuss the details of every detected line but instead present the data and highlight the rich chemistry provided by ALMA's new capabilities, in the nearby starburst galaxy NGC 253.* This paper complements two other studies of NGC 253 using the same data set, one describing the molecular outflow revealed in ^{12}CO emission (Bolatto et al. 2013a, hereafter B13) and the other constraining the molecular clump properties in the central starburst region

[10] Adjunct Astronomer at the National Radio Astronomy Observatory

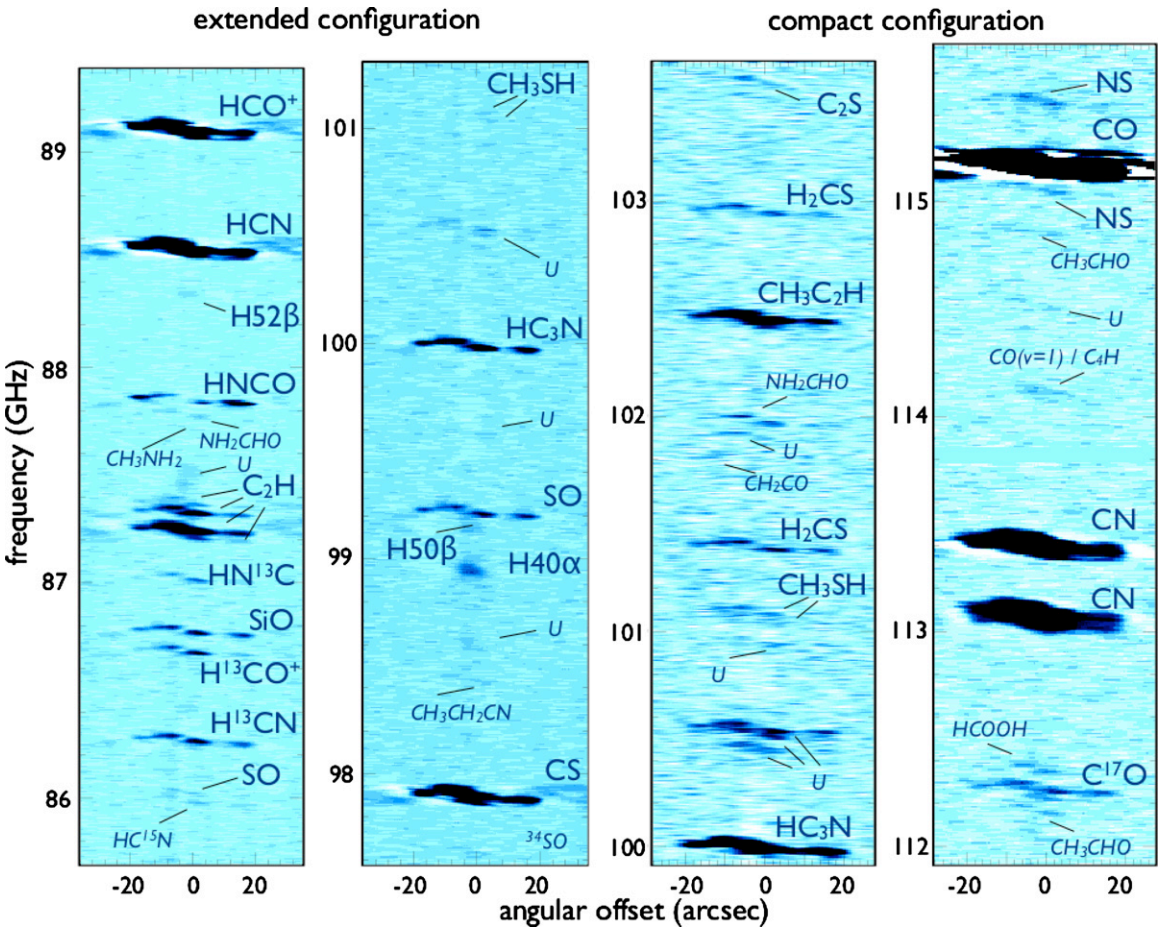

Figure 1. Position–velocity cut along the major axis of the central bar of NGC 253 (equivalent to an optical/near-infrared long-slit spectrum). Angular offsets are given with respect to the galaxy center. The left two panels show the lower and upper sidebands of the extended ALMA configuration, the right two panels the corresponding sidebands of the compact configuration. Identified molecular spectral lines are labeled (secure: bold, tentative: italics, see Table 1 for a full description of transitions). The CO line is completely saturated in this presentation and the HCN, HCO^+, and CN lines are partially saturated. Table 2 lists the coordinate about which the offsets are referenced.

using the brightest dense gas tracers available (Leroy et al. 2014, hereafter L14).

The paper is structured as follows: Section 2 briefly summarizes the observations, data reduction and data products. In Section 3 we present our identification of the rich suite of molecular line emission in the galaxy. We then proceed to sketch a simple picture of the conditions in the central region of NGC 253, by focusing on several groups of key molecular gas tracers (Section 4). We conclude by providing a short summary in Section 5. Throughout the paper we adopt a distance to NGC 253 of 3.5 Mpc (Rekola et al. 2005), i.e., 1″ corresponds to 17 pc at that distance. The systemic velocity of NGC 253 is ∼250 km s^{-1} (e.g., Houghton et al. 1997).

2. OBSERVATIONS AND DATA REDUCTION

Observations. We have mapped NGC 253 with ALMA in cycle 0 (16 antenna array) in two different frequency setups and configurations. Details regarding the observations and data reduction can be found in B13 and L14 and we here summarize the observational parameters that are most relevant for the current study. Both setups covered an instantaneous bandwidth of 8 GHz each: The first frequency setup, covering 85.6–89.6 GHz (lower side-band, LSB) and 97.4–101.4 GHz (upper side-band, USB), is a central 3–point mosaic along the major axis in the extended configuration (average beam size: ∼2″, ∼35 pc). This mosaic covers the central 1′ (1 kpc) of NGC 253's starburst. The second setup covers 99.8–103.7 GHz (LSB) and 111.8–115.7 GHz (USB) and is a 7–point mosaic of NGC 253's center in the compact configuration. This yields an average beam size of ∼4″ (∼70 pc) and a field of view of roughly 1.′5 (∼1.5 kpc).

Data reduction. All of the calibration and imaging of the data cubes was completed within CASA, including self-calibration to remove residual phase and flux calibration errors. After imaging, much of the remaining analysis was performed with IDL scripts with some use of the Miriad and Matlab software packages. Most of the data presented here is based on the continuum–subtracted cube, where the continuum was defined in those spectral regions where no line emission was evident. Our final cube has 20 km s^{-1} velocity resolution and a typical rms of ∼2.0 mJy $beam^{-1}$ (extended, LSB: 1.9 mJy, extended, USB: 2.1 mJy, compact, LSB: 2.0 mJy, compact, USB: 3.3 mJy).

Final data cubes. We display the information in the data cubes in two complementary fashions: through a position–velocity (pV) diagram along the major axis of NGC 253 in Figure 1; a representation similar to long-slit spectroscopy in optical/NIR astronomy (Figure 1). The second (Figure 2) is a single spectrum taken toward a central molecular peak (position 5). As outlined above, the data consist of four final data cubes, the LSB and USB cubes for the extended configuration, and those for the compact configuration. Figures 1 and 2 also show our line identification (see also Table 1), as further discussed in Section 3.

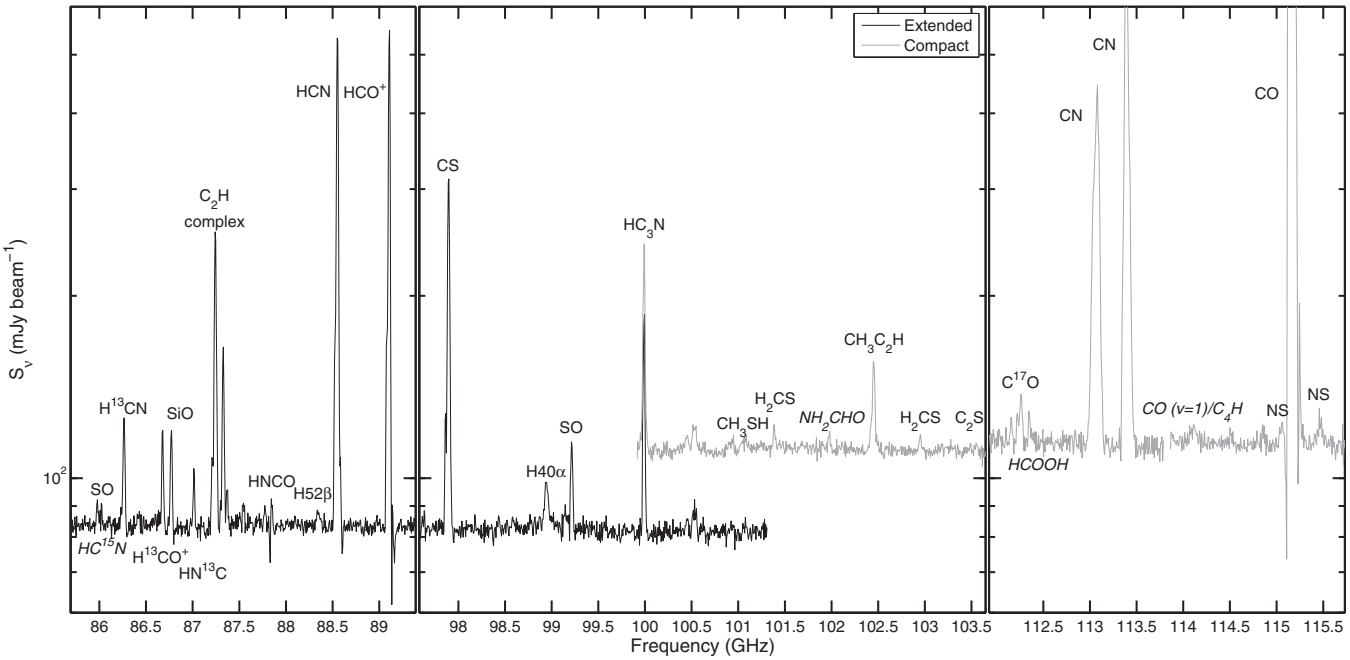

Figure 2. Extracted spectrum near the center of NGC 253 (position 5 in Figure 4), on a logarithmic scale. To deal with subtle issues regarding the bandpass calibration, the data have been independently continuum subtracted for each spectral window. After that, the average continuum flux density in a given spectral window was added to the spectrum. The flux density offset between the observations obtained in the compact and extended configurations is real; the observations in the compact configuration recover more of the extended flux. As in Figure 1, identified molecular spectral lines are labeled (secure: bold, tentative: italics, see Table 1 for full description of transitions).

Integrated line maps. We created line cubes for each line, and then blanked those with a mask derived from the CO(1–0) line (by far the brightest line in the bandpass). The integrated intensity map for a given line was then derived by simply adding all data in the respective data cube (without any further flux cutoff). Integrated line maps are corrected for primary beam attenuation and are shown in Figure 3.

Uncertainties. We calculated error maps by taking the number of channels per pixel into account. An inspection of the data cubes revealed that these error maps provide too optimistic uncertainties, as they do not account for artifacts (in particular the negative "bowl" due to the missing short spacings) in the current data. We thus adopt a conservative 10% error for pixels that have been detected at high S/N ($>$ 10), where the noise N is from taken from our error maps. For pixels that are detected at lower S/N ($5 < \mathrm{S/N} < 10$) we adopt an even more conservative 30% uncertainty, to also account for possible issues in baseline determination. We ignore all pixels that have a S/N < 5 in the analysis that follows. We present our line intensity measurements toward 10 positions in NGC 253 (Figure 4, coordinates in Table 2) in Table 3. Toward the center of the galaxy (in particular region 6, Figure 4) line emission is observed against strong continuum (L14). Some resulting absorption will decrease the integrated line signal at these locations. Because of this the fluxes toward this location should be considered highly uncertain.

Spatial filtering. As ALMA is an interferometer it acts as a spatial filter, sampling only a range of spatial scales. So the observations will potentially resolve out some flux. In the compact (extended) configuration spatial scales of 12–47 kλ (23–100 kλ) (90th percentile) were sampled, corresponding to 4.″4–18″ (2″–9″). Hence the observations should adequately sample fluxes uniform over ∼10″ (in one channel). The one exception to this is ^{12}CO(1–0), which has been zero-spacing corrected and therefore detects all flux (see discussion in B13). It is not possible to estimate the percentage of detected flux for every line in the survey because suitable single-dish observations are often not available. We do, however, determine this fraction for a number of transitions where possible. For the following transitions we calculate detected flux percentages over single-dish beam of ∼22 ″ – ∼28″ of: HCN(1–0)—100% (Paglione et al. 1995), HCO$^+$(1–0)—55% (Martín et al. 2009b), C^{17}O(1–0)—60% (Henkel et al. 2014), SiO(2–1)—110% (Martín et al. 2009b), CN(1–0;(3/2) – (1/2))—60% (Henkel et al. 2014), C$_2$H(1–0;(3/2) – (1/2))—60% (Nakajima et al. 2011), and HNCO(4_{04}–3_{03})—50% (Nguyen-Q-Rieu et al. 1991; though this value is highly uncertain because HNCO does not peak where Nguyen-Q-Rieu et al. pointed). Therefore, it appears that the data consistently detect at least 50% of their respective single dish fluxes. Furthermore our discussion focuses on the compact clumps of emission, where much higher fractions of the flux are detected ($\gtrsim$90%). (In fact, spatial filtering of the interferometer actually affords advantages because it allows the separation of these compact structures from any extended diffuse medium that can dominate single-dish observations.) Finally, we avoid comparing line intensities derived from different array configurations wherever possible in this study, to further mitigate against differences in resolved flux. Hence we conclude that uncertainties in line ratios due to different degrees of missing flux are $\lesssim$10%.

3. RESULTS

3.1. The Nucleus of NGC 253

The nucleus of NGC 253 is characterized by the inner portion of NGC 253's large-scale bar: The highly inclined ($i \simeq 78$ deg) nuclear disk extends from the very center out to a radius, $r \gtrsim 370$ pc. In some transitions emission is seen out to the edge of the mosaic. The outer part of the nuclear disk (the "outer nuclear disk") is suggested to represent the location where

Table 1
Observed Emission Lines

Transition	Rest Frequency (GHz)	Setup	Comments
$HC^{15}N(J = 1–0)$	*86.054*	ext, LSB	tent. ID
$SO(J_N = 2_2–1_1)$	86.09395	ext, LSB	
$H^{13}CN(1–0)$	86.34016	ext, LSB	
$HCO(J_{K_a K_c} = 1_{1,0}–0_{0,0})$	86.67076	ext, LSB	
$H^{13}CO^+(1–0)$	86.75429	ext, LSB	
$SiO(2–1; v = 0)$	86.84696	ext, LSB	
$HN^{13}C(1–0)$	87.09085	ext, LSB	
$C_2H(N = 1–0; J = 3/2–1/2)$	87.31690	ext, LSB	main C_2H FS component
$C_2H(1–0; 1/2–1/2)$	87.40199	ext, LSB	secondary C_2H FS component
U	*87.567*	ext, LSB	poss. ID: *SiN*(2–1; 5/2–3/2)
$CH_3NH_2(3_1–3_0)$	*87.785*	ext, LSB	tent. ID
$NH_2CHO(4_{1,3}–3_{1,2})$	*87.853*	ext, LSB	tent. ID
$HNCO(4_{0,4}–3_{0,3})$	87.92524	ext, LSB	
$H(52)\beta$	88.40569	ext, LSB	
HCN(1–0)	88.63160	ext, LSB	
$HCO^+(1–0)$	89.18852	ext, LSB	
$^{34}SO(3_2–2_1)$	*97.720*	ext, USB	tent. ID
CS(2–1)	97.98095	ext, USB	
CH_3CH_2CN	*98.525*	ext, USB	tent. ID; blend: $(11_6–10_7)$ & $(11_7–10_7)$
U	*98.667*	ext, USB	no obvious ID
$H(40)\alpha$	99.02295	ext, USB	
$H(50)\beta$	99.22521	ext, USB	
$SO(3_2–2_1)$	99.29987	ext, USB	
U	*99.669*	ext, USB	no obvious ID
$C_2S(7_8–6_7)$	99.86651	ext, USB	
$HC_3N(11–10)$	100.07640	ext, USB, comp, LSB	
U	*100.542*	ext, USB, comp, LSB	poss. ID: $CH_2CN(5_{2,3}–4_{2,2}; 9/2–7/2)$
U	*100.612*	ext, USB, comp, LSB	poss. IDs: $CH_2CN(5_{0,5}–4_{0,4}; 9/2–7/2)$ $CH_3CH_2CN(11_{1,10}–10_{1,9})$
U	*100.632*	ext, USB, comp, LSB	poss. IDs: $NH_2CN(5_{1,4}–4_{1,3})$; $CH_2CN(5_{2,4}–4_{2,3}; 11/2–9/2)$
U	*100.992*	ext, USB, comp, LSB	poss. ID: $CH_3CH_2OH(8_{2,7}–8_{18})$
$CH_3SH(4_0–3_0)A^+E$	101.13916	ext, USB; comp, LSB	
$CH_3SH(4_2–3_2)A$	*101.180*	ext, USB; comp, LSB	tent. ID
$H_2CS(3_{1,3}–2_{1,2})$	101.47788	comp, LSB	ortho-H_2CS
$CH_2CO(5_{1,4}–4_{4_{1,3}})$	*101.892*	comp, LSB	tent. ID
U	*101.988*	comp, LSB	no obvious ID
$NH_2CHO(5_{1,5}–4_{1,4})$	*102.070*	comp, LSB	tent. ID
$CH_3C_2H(6_k–5_k)$	102.54798	comp, LSB	
H_2CS	103.04054	comp, LSB	para: $(3_{2,2}–2_{2,1})$, $(3_{0,3}–2_{0,2})$, $(3_{2,1}–2_{2,0})$
$C_2S(8_8–7_7)$	103.64075	comp, LSB	
$CH_3CHO(6_{1,5}–5_{1,5})A^+$	*112.247*	comp, USB	tent. ID
$C^{17}O(1–0)$	112.35928	comp, USB	
HCOOH	*112.459*	comp, USB	tent. ID, blend: $(5_{3,3}–4_{3,2})$ & $(5_{3,2}–4_{3,1})$
CN(1–0;1/2–1/2)	113.19128	comp, USB	secondary CN FS group
CN(1–0;3/2–1/2)	113.49097	comp, USB	main CN FS group
U	*114.218*	comp, USB	poss. IDs: CO(1–0; $v = 1$); $C_4H(12–11; 25/2–23/2 \& 23/2–21/2)$
U	*114.605*	comp, USB	no obvious ID
$CH_3CHO(6_{0,6}–5_{0,5})A^{++}E$	*114.952*	comp, USB	
NS(5/2–3/2;7/2–5/2)	115.15394	comp, USB	blended with CO
CO(1–0)	115.27120	comp, USB	Bolatto et al. 2013a
NS(5/2–3/2;7/2–5/2)	115.55625	comp, USB	

Notes. Species in italics represent tentative identifications. In these cases, the frequency listed is the observed one corrected to rest frequency based on the known velocity field and does not reflect the rest frequency of the tentatively identified line. Lines labeled *U* are the ones that we could not securely identify, and in some cases we give possible ID's in the last column.

gas flowing radially inward along the large-scale bar collects between the outer and inner Lindblad resonance (García-Burillo et al. 2000: Paglione et al. 2004). Embedded within the outer disk is a compact ($r \simeq 170$ pc) region exhibiting a large quantity of high density gas and intense star formation, which is discussed in detail in Section 4.2. A molecular gas outflow/wind is being driven from this inner nuclear disk, as discussed in B13.

We have selected 10 individual locations that span the nuclear disk and the base of the molecular outflow in NGC 253 (Table 2). Regions 3–9 trace the inner starburst disk from west to east and

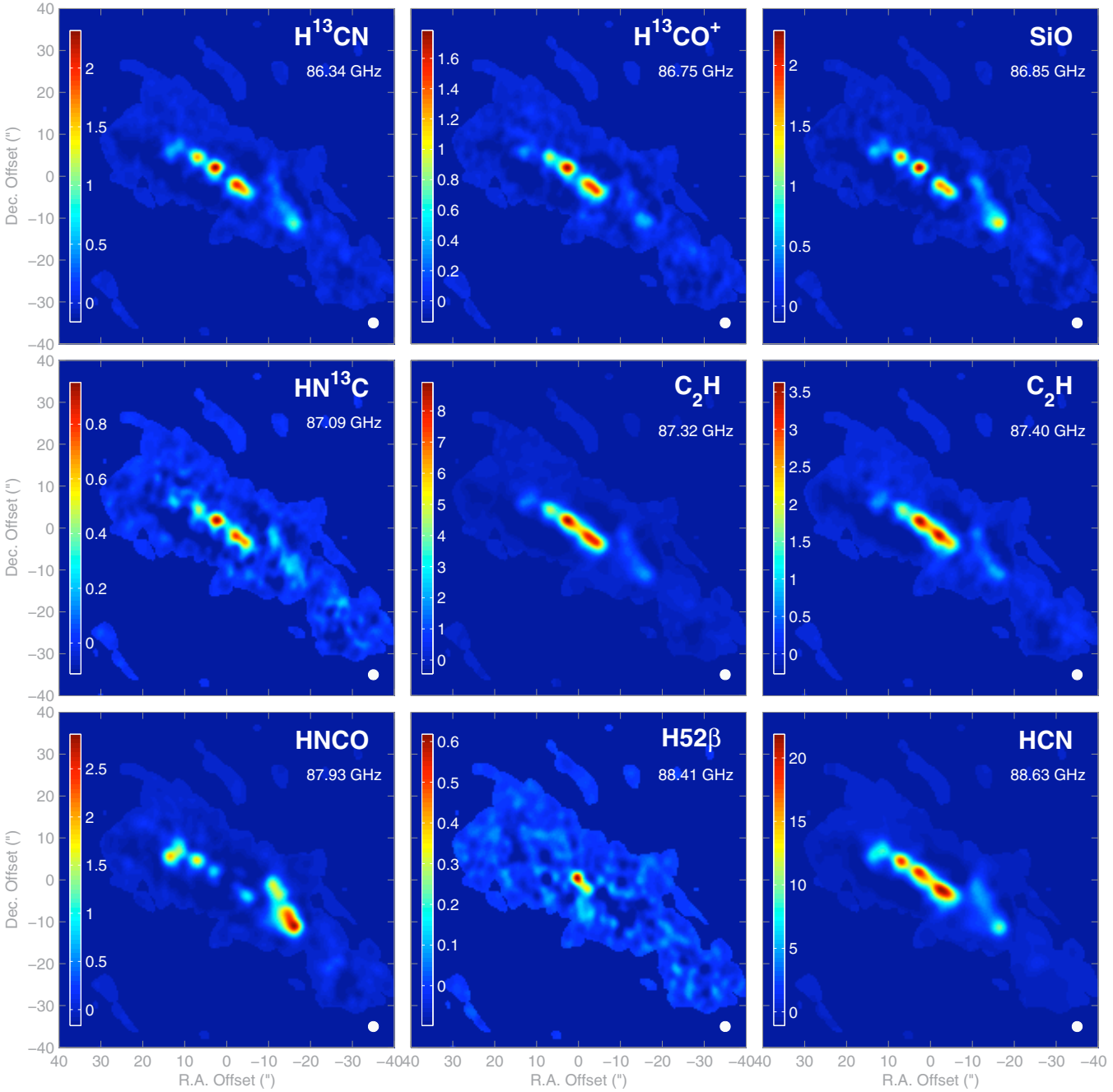

Figure 3. Integrated intensity maps of selected molecules in our observations (Table 1). The respective intensity scale (in units of K km s^{-1}) is shown in each panel. The name of the line and its rest frequency are given in the top right corner of each panel. The beam size is shown in the bottom right corner. Tentatively identified lines are labeled in italics.

regions 5 and 6 are coincident with the detected millimeter continuum emission in the galaxy (L14). Regions 1 and 10 are located at the western and eastern base of the southern molecular outflow (B13). Region 2 indicates the shocked region toward the north. The GMC physical properties in these regions are discussed in detail in L14. We further caution that some of our line measurements toward region 6 (the center) may be affected by absorption and continuum subtraction uncertainties (as discussed in Section 2).

In Table 1 we provide a summary of all detected lines (column 1), their rest frequencies (column 2), and observational setup (column 3). For each of our 10 regions, we measure the peak integrated intensity (in K km s^{-1}) at that position and report the values in Table 3. We measure all values from beam–matched maps, i.e., all the compact and extended configuration data have been convolved to a common resolution, respectively (this common resolution is given in column 4 of Table 3, whereas column 3 gives the original resolution). We have discussed our uncertainty estimates in Section 2. Table 3 also includes the intensity measurement in each transition for the entire galaxy (columns 5 and 6).

3.2. Molecular Emission Across NGC 253's Nucleus

Figure 1 shows the position–velocity (pV) diagram oriented along the molecular bar (i.e., along the major axis of the galaxy)

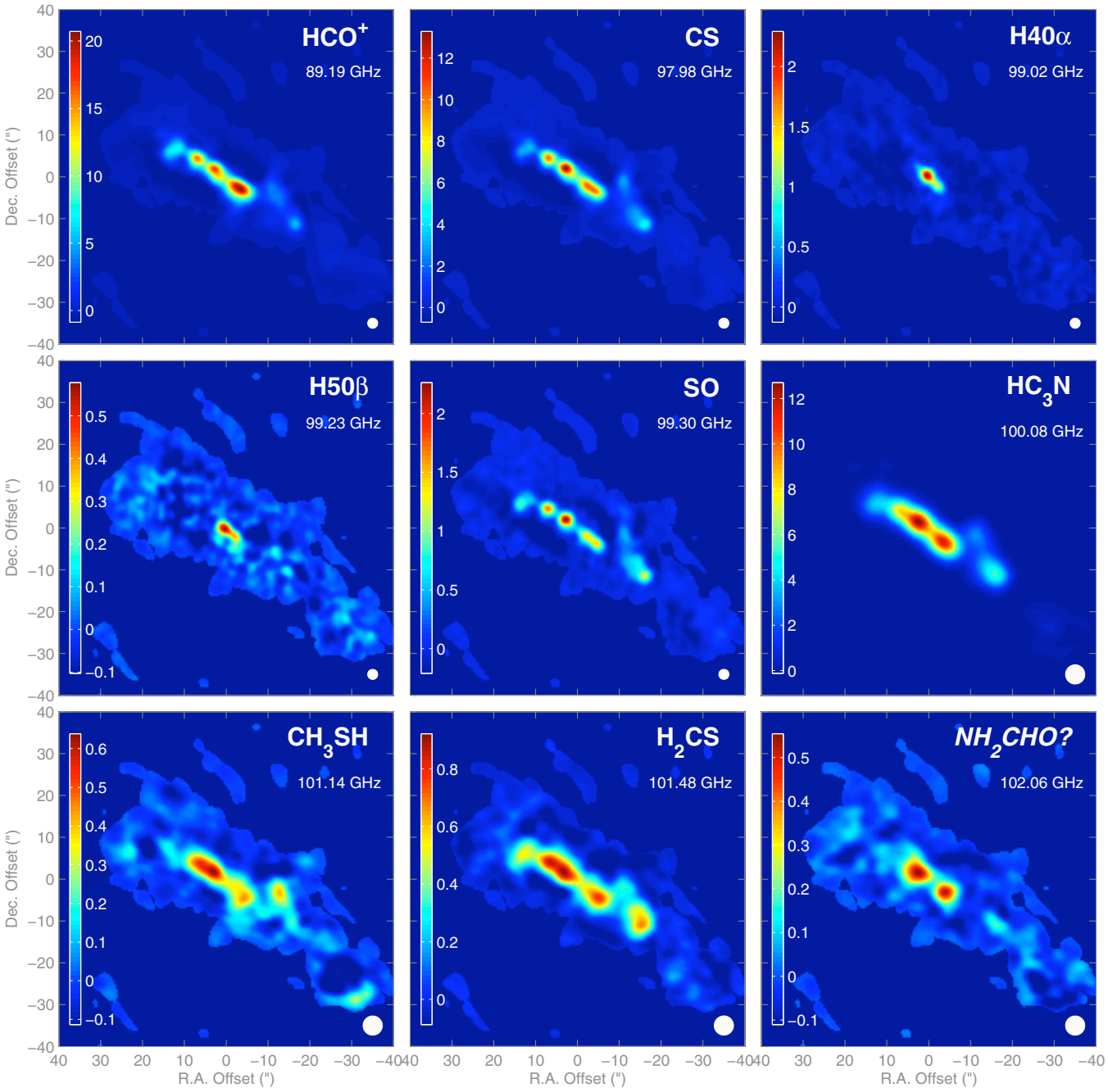

Figure 3b. (Continued)

of all four data cubes. This figure shows the richness of the ALMA data cubes, and the challenges in finding the correct line identification. Already from this presentation it is clear that the emission of the different line species emerge from different regions in the galaxy.

We detect at least 50 emission lines in total of which 27 have unambiguous identifications. This corresponds to a detection ratio of one line every ∼0.25 GHz. Species printed in *italics* are tentative IDs (13 lines). These lines have clear candidate transitions from a species not yet well established in extragalactic systems (see Section 3.3). The candidate IDs are given in column 4 of Table 1. In some cases we were not able to find a plausible line identification or the broadness of the spectral line prohibited a unique identification. Those lines are labeled *U* (unidentified; 10 cases). In those cases we give our best estimate for each feature's rest frequency in column 2.

We show line maps for 27 of the bright, unblended lines in Figure 3. In Figure 4 we select out six species that summarize the basic morphological patterns seen in the sample. Each represent key tracers of the different phases of the molecular gas, as discussed below. These are ^{12}CO, a tracer for the overall molecular gas distribution, $^{12}C^{17}O$, an optically thin tracer of molecular gas emission, C_2H, a photon-dominated region (PDR) tracer, H40α, a hydrogen recombination line and H II region tracer, HCN, a high-density gas tracer and HNCO, a weak shock tracer.

From Figures 3 and 4 it is apparent that the morphologies change significantly between species (as is already evident from Figure 1). Molecular gas column densities remain quite large

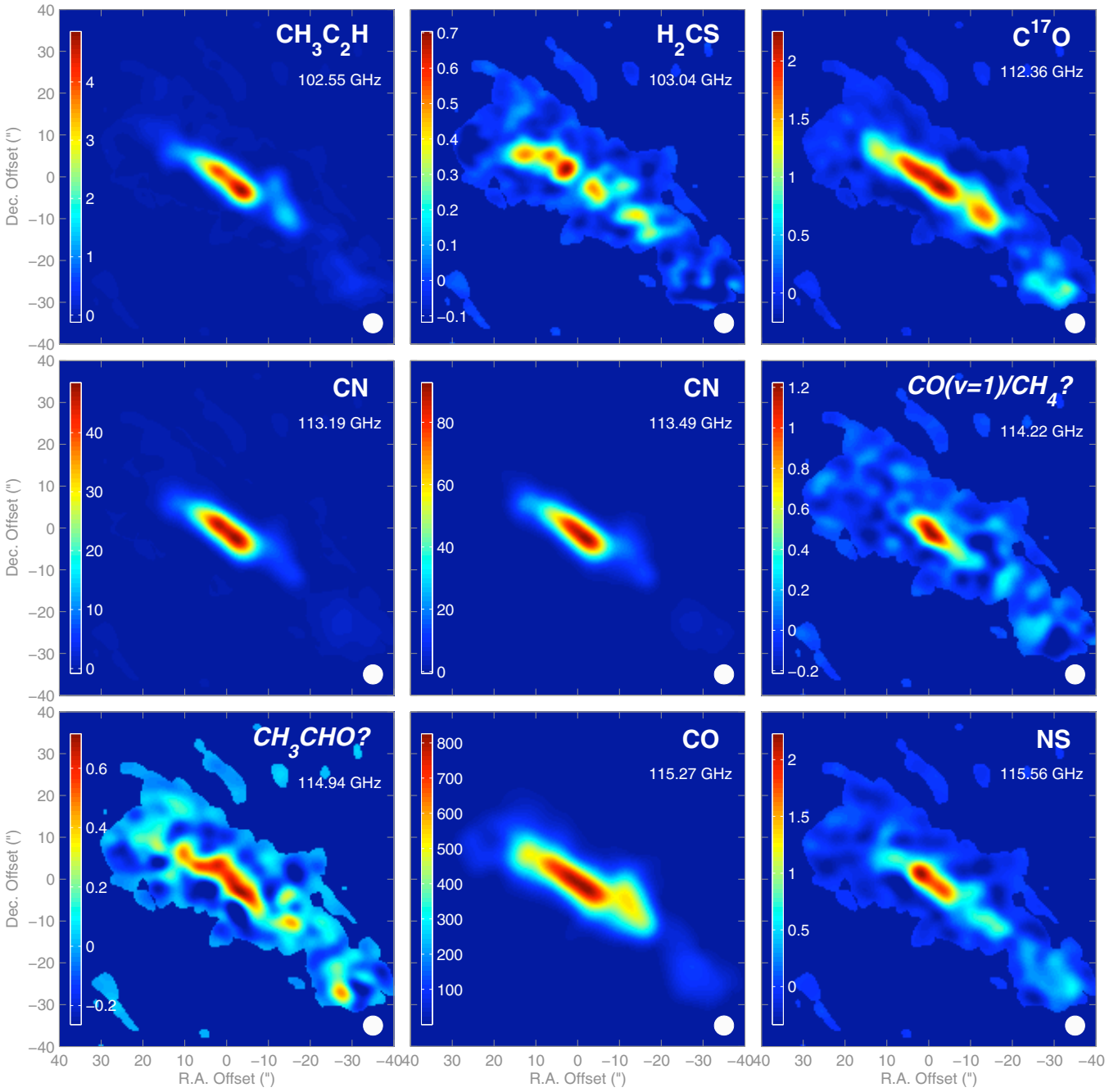

Figure 3c. (Continued)

across the entire nuclear disk, maintaining $N(H_2) \gtrsim 10^{23}$ cm^{-2} over much of the disk (Section 3.4). The wide range of dense gas tracers observed demonstrates that dense gas is present across much of this region, but the dense gas fraction increases toward the inner disk (L14). The millimeter hydrogen recombination lines, including for the first time Hβ lines, show that dense H II regions associated with the young starburst (or possibly active galactic nucleus; Mohan et al. 2002) are confined to the innermost part of this inner disk. Species like C_2H, CN, and CH_3C_2H also dominate from this inner nuclear disk. HNCO, on the other hand, is dominated by the outer nuclear disk.

The brightest and most widespread transitions (HCN, HCO^+, and CN) show weak emission extended vertically between 1 and 2, following the base of the molecular outflow, suggesting there is dense molecular gas here. However, we do not discuss the dense gas tracers in the outflow in detail here due to the difficulties dealing with the morphology of the maps above and below the disk in the presence of the negative "bowl."

3.3. Tentative and Unidentified Lines

There are a number of detected lines for which no clear identification was possible. We have listed tentative identifications in Table 1—in some cases no plausible species were found, and these lines constitute unidentified (*U*) lines. The majority of these tentative identifications (but not tentative detections) match prominent transitions from larger molecules, including the aldehydes CH_3CHO and NH_2CHO, cyanides CH_2CN and CH_3CH_2CN, and a number of organics of similar complexity,

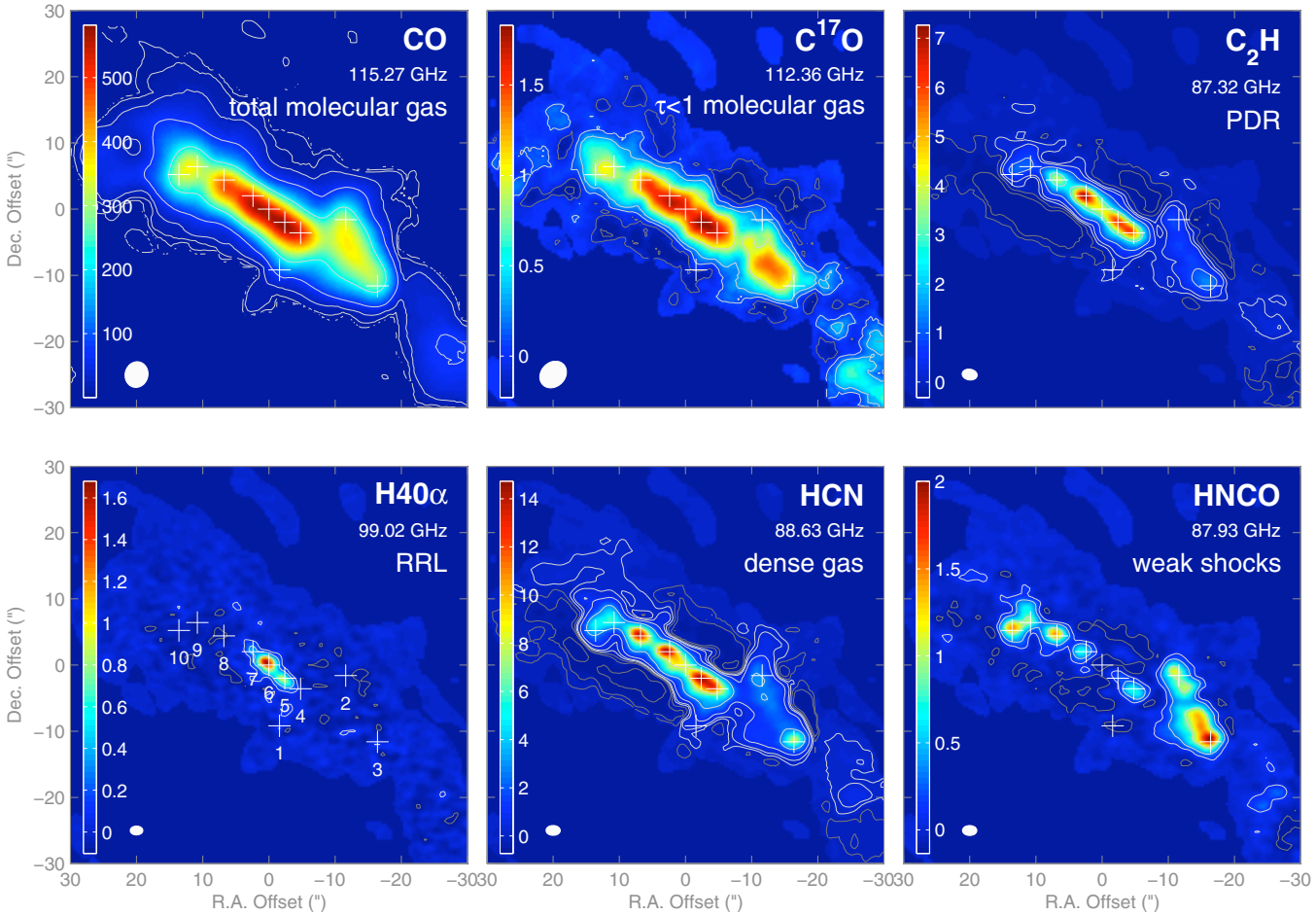

Figure 4. Collection of key molecular gas tracers in NGC 253. From top left to bottom right: CO(1–0) (main molecular gas tracer), $C^{17}O$(1–0) (optically thin tracer of the molecular gas), C_2H (PDR tracer), H40α (radio recombination line), HCN (high density gas tracer), HNCO (shock tracer). The crosses and labels (bottom left panel) mark the different regions defined in the galaxy. Logarithmic contours start at 1 K km s^{-1} and increase/decrease (white/gray) by a factor of three from one contour to the next. The beam size is indicated in the bottom left corner of each panel.

Table 2
NGC 253 Positions

Region	R.A. (2000.0)	Decl. (2000.0)
1	00 47 33.041	−25 17 26.61
2	00 47 32.290	−25 17 19.10
3	00 47 31.936	−25 17 29.10
4	00 47 32.792	−25 17 21.10
5	00 47 32.969	−25 17 19.50
6	00 47 33.159	−25 17 17.41
7	00 47 33.323	−25 17 15.50
8	00 47 33.647	−25 17 13.10
9	00 47 33.942	−25 17 11.10
10	00 47 34.148	−25 17 12.30
Map	00 47 33.100	−25 17 17.50

Notes. Coordinates of the 10 regions in NGC 253 (indicated in Figure 4) for which intensities have been measured (see Table 3). The coordinates of (0, 0) reference position of the maps is also given.

CH_2CO, HCOOH, and CH_3CH_2OH. These molecules are abundant in the Galactic center (e.g., Cummins et al. 1986) and are expected to be detectable at our sensitivity in NGC 253. If follow-up, multi-line studies confirm these IDs then they would represent their first extragalactic detections.

3.4. Excitation and Abundances

When appropriate, an estimate of abundances is made for the detected species. Molecular column densities $N_{\rm mol}$ are determined assuming optically thin LTE emission:

$$N_{\rm mol} = \left(\frac{3kQe^{E_u/kT_{ex}}}{8\pi^3\nu S_{ul}\mu_0^2 g_u}\right) I_{\rm mol}, \quad (1)$$

where S_{ul} is the line strength, and g_u and E_u are the upper state degeneracy and energy, respectively, Q is the partition function, μ_o is the dipole moment in debye, and $T_{\rm ex}$ is the excitation temperature associated with the transition (e.g., Turner 1991). For the symmetric (CH_3SH) and asymmetric (HNCO, H_2CS) tops Q is proportional to $T_{\rm ex}^{3/2}$, whereas Q for the linear rotors (the rest) is proportional to $T_{\rm ex}$.

To calculate abundances it is necessary to adopt an $T_{\rm ex}$. Since this survey covers only one band, gas excitation is not the focus of this project. The only lines that are detected and directly constrain gas excitation is a pair of SO transitions, SO(3_2–2_1) and SO(2_2–1_1). From this pair, an excitation temperature is estimated via

$$T_{\rm ex} = \frac{10.09\ {\rm K}}{ln\left(\frac{R}{2.18}\right)}, \quad (2)$$

where R is the intensity ratio, SO(3_2–2_1)/SO(2_2–1_1). Toward the inner nuclear disk this ratio has a value of $R \simeq 2.5$. There is some

Table 3
Line Intensities

Transition	Beam ($''$)	I(1)	I(2)	I(3)	I(4)	I(5)	I(6)	I(7)	I(8)	I(9)	(I10)
						(K km s^{-1})					
SO($J_N = 2_2$–1_1)	2.0/2.4	<5.7	< 5.7	<7.2	6.0 ± 1.8	12.0 ± 3.6	<7.2	19.5 ± 1.9	<5.7	<5.7	<5.7
$H^{13}CN$(1–0)	2.0/2.4	<5.7	8.5 ± 2.6	25.3 ± 2.5	39.6 ± 4.0	58.4 ± 5.8	<7.1	64.3 ± 6.4	45.3 ± 4.5	11.7 ± 1.2	13.4 ± 1.3
HCO($J_{K_aK_c} = 1_{1,0}$–$0_{0,0}$)	1.9/2.4	<5.6	<5.6	<7.1	8.2 ± 2.5	<7.1	<7.1	<7.1	<5.6	<5.6	<5.6
$H^{13}CO^+$(1–0)	1.9/2.4	<5.6	<5.6	8.7 ± 2.6	37.8 ± 3.8	41.7 ± 4.2	11.0 ± 3.3	49.1 ± 4.9	26.8 ± 2.7	<5.6	7.3 ± 2.2
SiO(2–1; $v = 0$)	1.9/2.4	<5.6	15.8 ± 1.6	36.6 ± 3.7	41.6 ± 4.2	48.1 ± 4.8	<7.0	62.7 ± 6.3	46.4 ± 4.6	13.2 ± 1.3	14.3 ± 1.4
$HN^{13}C$(1–0)	1.9/2.4	<5.6	5.9 ± 1.8	<7.0	17.3 ± 1.7	22.1 ± 2.2	7.3 ± 2.2	26.6 ± 2.7	13.1 ± 1.3	<5.6	<5.6
C_2H($N = 1$–$0;J = 3/2$–$1/2$)	1.9/2.4	<5.6	27.3 ± 2.7	46.2 ± 4.6	194.8 ± 19.5	224 ± 22	157 ± 16	246 ± 25	133 ± 13	36.5 ± 3.6	30.9 ± 3.1
C_2H(1–0;1/2–1/2)	1.9/2.4	6.7 ± 2.0	15.0 ± 1.5	19.4 ± 1.9	67.2 ± 6.7	95.3 ± 9.5	69.7 ± 7.0	98.9 ± 9.9	49.7 ± 5.0	14.4 ± 1.4	12.8 ± 1.3
HNCO($4_{0,4}$–$3_{0,3}$)	1.8/2.4	<5.5	43.1 ± 4.3	67.8 ± 6.8	25.5 ± 2.6	7.1 ± 2.1	<5.5	19.5 ± 1.9	46.4 ± 4.6	33.5 ± 3.3	50.0 ± 5.0
H(52)β	1.8/2.4	<5.4	<4.1	<5.4	<4.1	9.0 ± 2.7	14.9 ± 1.5	<5.4	<5.4	<4.1	<4.1
HCN(1–0)	1.8/2.4	24.0 ± 2.4	119 ± 12	265 ± 27	435 ± 44	582 ± 58	360 ± 36	526 ± 53	512 ± 51	211 ± 21	179 ± 18
HCO^+(1–0)	1.8/2.4	26.7 ± 2.7	75.5 ± 7.5	137 ± 14	432 ± 43	512 ± 51	276 ± 27.6	450 ± 45	422 ± 42.	176 ± 18	153 ± 15
CS(2–1)	1.6/2.4	<4.4	57.2 ± 5.7	99.7 ± 10.0	208 ± 21	233 ± 23	136 ± 14	287 ± 29	225 ± 23	63.4 ± 6.3	53.0 ± 5.3
H(40)α	1.6/2.4	<3.2	<3.2	<4.3	<3.2	25.1 ± 2.5	47.6 ± 4.8	13.0 ± 1.3	<3.2	<3.2	<3.2
H(50)β	1.6/2.4	<4.3	<3.2	<4.3	<3.2	7.8 ± 2.3	12.1 ± 1.2	<4.3	<4.3	<3.2	<3.2
SO(3_2–2_1)	1.6/2.4	<4.3	10.3 ± 1.0	24.5 ± 2.5	30.1 ± 3.0	30.3 ± 3.0	12.1 ± 1.2	46.9 ± 4.7	35.5 ± 3.6	10.8 ± 1.1	17.2 ± 1.7
HC_3N(11–10)	4.1/4.6	<2.0	16.2 ± 1.6	29.4 ± 2.9	60.7 ± 6.1	59.9 ± 6.0	52.8 ± 5.3	72.0 ± 7.2	48.0 ± 4.8	23.2 ± 2.3	19.7 ± 2.0
CH_3SH(4_0–3_0)A^+E	4.2/4.6	<2.0	<2.0	<2.3	2.3 ± 0.7	<2.3	<2.3	3.4 ± 1.0	2.8 ± 0.8	<2.0	<2.0
H_2CS($3_{1,3}$–$2_{1,2}$)	4.2/4.6	<2.0	<2.0	3.1 ± 0.9	4.1 ± 0.4	3.1 ± 0.9	3.4 ± 1.0	4.8 ± 0.5	4.8 ± 0.5	2.6 ± 0.8	2.8 ± 0.8
CH_3C_2H(6_k–5_k)	4.2/4.6	<1.9	5.8 ± 0.6	5.4 ± 0.5	24.2 ± 2.4	24.8 ± 2.5	20.9 ± 2.1	21.5 ± 2.1	11.9 ± 1.2	6.2 ± 0.6	4.4 ± 0.4
H_2CS	4.1/4.6	<1.9	<1.9	<2.2	2.5 ± 0.8	2.2 ± 0.7	<2.2	3.8 ± 1.1	2.8 ± 0.8	2.2 ± 0.7	2.6 ± 0.8
$C^{17}O$(1–0)	4.0/4.6	<2.7	<2.7	3.9 ± 1.2	9.2 ± 0.9	10.2 ± 1.0	9.5 ± 0.9	9.1 ± 0.9	7.0 ± 0.7	5.0 ± 1.5	4.2 ± 1.2
CN(1–0;1/2–1/2)	4.0/4.6	4.9 ± 1.5	18.0 ± 1.8	23.1 ± 2.3	169 ± 17	215 ± 22	201 ± 20	196 ± 20	107 ± 11	42.8 ± 4.3	30.4 ± 3.0
CN(1–0;3/2–1/2)	4.0/4.6	27.6 ± 2.8	58.0 ± 5.8	52.9 ± 5.3	322 ± 32	403 ± 40.3	380 ± 38	325 ± 32	206 ± 21	109 ± 11	81.9 ± 8.2
CO(1–0)	3.7/4.6	718 ± 72	1920 ± 190	1570 ± 160	3200 ± 320	3550 ± 360	3410 ± 340	3130 ± 310	2710 ± 270	2160 ± 220	1920 ± 190
NS(5/2–3/2;7/2–5/2)	3.7/4.6	<3.2	<3.2	<3.9	6.9 ± 0.7	7.8 ± 0.8	8.1 ± 0.8	9.2 ± 0.9	3.4 ± 1.0	<3.2	<3.5

Notes. Integrated intensity measurements at positions 1–10 and intensity of the entire galaxy. *Column 1:* The transition. *Column 2:* The original resolution of the ALMA data/common resolution used in this study. *Column 3-12:* The integrated intensity for regions #1–#10 (see Figure 4 for location of regions) with uncertainty. Uncertainties are set to 10%, representing absolute flux calibration uncertainties only, unless S/N is low then they are conservatively set to 30% (see Section 2). Small errors associated with missing flux are not included. We caution that values for region 6 may be affected by absorption toward the central continuum source. All upper limits are 5σ.

evidence for the ratio to increase toward the outer nuclear disk ($R \lesssim 4$), but the faintness of SO(2_2–1_1) limits what can be said. For these ratios, we estimate the inner disk to have an excitation temperature of 74 K in SO, dropping to $T_{ex} \lesssim 17$ K. Indirect methods of estimating T_{ex} can also be achieved by radiative transfer modeling (see Section 4.2). There T_{ex} is found to range between ~6–45 K. Therefore, T_{ex} likely falls between at least 10–75 K, across much of the nuclear region. Ott et al. (2005) use NH_3 to estimate gas kinetic temperatures, T_{kin}, across the inner nuclear disk of approximately twice the 74 K measured here, however Knudsen et al. (2007) (and this paper) favor T_{kin} nearer this value for HCN and HCO^+ (see Section 4.2). The drop in T_{ex} toward the outer nuclear disk region reflects SO becoming more strongly sub-thermal in lower density gas.

The relevant excitation temperature for a given species/transition depends on a number of factors, including gas density, opacity, molecular structure and location within the nucleus. For transitions with effective critical densities significantly above the gas density, T_{ex} will be lower than the T_{kin} (subthermal excitation). Changes in n_{H_2} and T_{kin} with position in the nucleus imply changes in excitation. The effective critical density of a species depends on line opacity, τ, (photons become an effective "collision" partner) and hence abundances, with high opacity lowering critical densities, n_{cr}, roughly in proportion to τ. Finally, even in the case that a transition is thermalized, the LTE calculated columns are strict upper limits because it assumes that all transitions of the molecule are thermalized up to arbitrarily high energies.

With these caveats stated, abundances are the important astrochemical variable and so we report "reference" ranges. In Table 4, abundances are reported for T_{ex} ranging from 10 K (first number in each entry) to 75 K (second number). Also included in the table are n_{cr} (not including opacity effects) for the transitions. It is expected that for the inner nuclear disk positions transitions with moderate n_{cr} (e.g., $C^{17}O$, HNCO, H_2CS, C_2H, HCO^+, and SO) will have T_{ex} at the high end of the range. High n_{cr} transitions and outer nuclear disk locations likely will have T_{ex} (and hence abundances) at the low end of the range. Future, follow up, multi-line studies of different species are necessary to narrow these quoted "reference" value ranges.

To convert N_{mol} to fractional abundances we also require H_2 column density, $N(H_2)$. $N(H_2)$ is most easily obtained from the CO(1–0) brightness and an empirical conversion factor, X_{CO}. We adopt a CO-to-H_2 conversion factor of $X_{CO} = 0.5 \times 10^{20}$ cm^{-2} (K km s^{-1})$^{-1}$. This is a factor of four lower than typical for the Galactic disk (Strong et al. 1988; Hunter et al. 1997; Bolatto et al. 2013b), but consistent with what has been previously estimated for NGC 253 (e.g., Paglione et al. 2001; B13; L14). Uncertainties in X_{CO} are significant, likely at the $\pm 2\times$ level, and in Section 4.1 some discussion of its validity in the context of optical thin $C^{17}O$(1–0) is discussed.

4. DISCUSSION

In the following we present a broad discussion of the chemistry in the nuclear region of NGC 253. The primary goal is to obtain spatially resolved views of the different molecular environments in and around the starburst center.

We begin our discussion by studying the main tracer of the molecular gas, ^{12}CO, its isotopologues, and implied molecular gas opacity in Section 4.1. In Section 4.2 we continue with a similar discussion of the isotopologues of the main tracers of the dense molecular gas phase ($H^{13}CN$, $H^{13}CO^+$, $HN^{13}C$). This is followed by a discussion of tracers of PDRs, (Section 4.3), shock tracers (HNCO and SiO; Section 4.4), Sulfur species (Section 4.5), hydrogen recombination lines (Section 4.6), and other tentatively identified species (Section 4.7) detected in our study. A schematic picture summarizes the overall chemistry of the central region of NGC 253 in the conclusions/summary section (Section 5).

4.1. CO Isotopologues and Gas Opacity

Our data cover a number of isotopologues (i.e., molecules where one atom is replaced with an isotope). Given the fact that atomic isotopes are much less abundant than the main atom, many of these isotopologue lines have low optical depth compared to the main species. Isotopologue ratios thus provide insights into the optical depth of the main lines and can also be used to constrain isotopic abundance ratios. The isotopic abundance ratio ultimately can provide insights into stellar nucleosynthesis and possible variations of the stellar initial mass function. In the discussion that follows we do not interpret the sometimes anomalous line ratios found for region 6 (i.e., the region that is coincident with the central continuum emission) as it is likely that in some cases our measurements are affected by absorption (Section 2).

A comparison of the brightness of the $C^{17}O$(1–0) transition to the ^{12}CO(1–0) transition [hereafter CO(1–0)] can provide important constraints on the total H_2 column. Being an optically thin version of CO, even in this extreme star formation environment, it permits CO abundances to be determined by "counting molecules" if the [CO/$C^{17}O$] abundance ratio is known.

The [CO/$C^{17}O$] abundance ratio is constrained based on existing measurements and nucleosynthetic expectations. In the Galaxy, [CO/$C^{17}O$] is $\lesssim$1900 at the solar radius and drops to ~900 in the Galactic center (e.g., Wilson & Rood 1994; Ladd 2004; Wouterloot et al. 2008). This decrease in the [CO/$C^{17}O$] abundance is consistent with ^{17}O being a secondary chemical evolution product formed from reactions between primary ^{16}O and a proton in intermediate mass stars. Therefore, in a strongly processed location like the center of a starburst, a low value of the CO/$C^{17}O$ abundance ratio is expected, so we adopt [CO/$C^{17}O$] = 1000, which is approximately the Galactic center value referenced above, as our nominal value.

As shown in Figure 5, this isotopologue line ratio is fairly constant with position in NGC 253 and large ($\gtrsim$350). For a ratio $^{16}O/^{17}O$ of 1000 in NGC 253, the measured ratio nominally implies a ^{12}CO opacity of ~2.5, a moderate value for the main CO line. Raising the intrinsic $^{16}O/^{17}O$ abundance to 2000 gives a ^{12}CO opacity of order ~5.5.

Various non-LTE effects can occur in a starburst environment that could alter the observed CO/$C^{17}O$ line ratio. Examples that artificially inflate the CO/$C^{17}O$ line ratio include: (1) CO has a higher excitation temperature than $C^{17}O$ because CO has high opacity and its emission is dominated by warmer, externally heated edges of the GMCs while $C^{17}O$ is dominated by the cooler interiors. (2) Isotope–selective photo-dissociation makes the cloud sizes smaller in $C^{17}O$ than CO. Or, (3) due to the absence of radiative trapping in $C^{17}O$, $C^{17}O$ is subthermal relative to CO and therefore fainter (e.g., Meier & Turner 2001). The first two would be expected to be pronounced close to the nuclear star formation. However, interestingly, no evidence is seen for an increase in the CO/$C^{17}O$ ratio toward the inner disk, where PDRs are enhanced (Section 4.3) and warm gas dominates. But if there is a decrease in density away from the inner disk then the third option can operate in the outer disk, partially compensating for the first two. For CO/^{13}CO

Table 4
LTE "Reference" Molecular Abundances for NGC 253[a]

Mol.	n_{cr}[b]	1	2	3	4	5	6	7	8	9	10
$H^{13}CN$	6.48	<0.2–<1(-9)	1–8(−10)	0.4–2(−9)	0.4–2(−9)	0.5–3(−9)	<0.6–<3(−10)	0.6–3(−9)	0.5–3(−9)	2–9(−10)	0.2–1(−9)
$H^{13}CO^+$	5.33	<0.1–<8(−10)	0.5–3(−9)	0.8–4(−10)	0.2–1(−9)	0.2–1(−9)	0.6–3(−10)	0.3–2(−9)	2–9(−10)	<0.7–<4(−10)	0.7–4(−10)
SiO	5.48	<0.3–<1(−9)	0.3–1(−9)	0.7–3.0(−9)	0.5–2(−9)	0.5–2(−9)	<0.8–<3(−10)	0.7–3(−9)	0.6–3(−9)	0.2–1(−9)	0/3–1(−9)
$HN^{13}C$	5.62	<0.3–<2(−9)	1–6(−10)	<1–<7(−10)	0.2–1(−9)	0.8–4(−9)	0.8–4(−10)	0.3–1(−9)	0.2–9(−10)	<0.9–<5(−10)	<<1–5(−10)
C_2H	5.27	<0.4—<2(−8)	1–5(−8)	2–8(−8)	0.4–2(−7)	0.4–2(−7)	0.3–2(−7)	0.5–3(−7)	0.3–2(−7)	1–6(−8)	1–5(−8)
HNCO	5.20	<0.1–<1(−8)	0.4–3(−8)	0.6–5(−8)	0.1–1(−8)	0.3–3(−9)	<0.3–<2(−9)	1–9(−9)	0.3–2(−8)	0.3–2(−8)	0.5–4(−8)
HCN	6.42	1–5(−9)	0.2–1(−8)	0.4–2(−8)	0.4–2(−8)	0.5–3(−8)	0.3–2(−8)	0.5–3(−8)	0.6–3(−8)	0.3–2(−8)	0.3–2(−8)
HCO^+	5.37	0.7–4(−9)	0.7–4(−9)	1–7(−9)	0.2–1(−8)	0.3–1(−8)	1–7(−9)	0.3–1(−8)	0.4–2(−8)	0.2–8(−9)	1–7(−9)
CS	5.78	<0.5–<2(−9)	2–9(−9)	0.4–2(−8)	0.5–2(−8)	0.5–2(−8)	0.3–1(−8)	0.7–3(−8)	0.6–3(−8)	0.3–1(−8)	2–9(−9)
SO	5.47	<2–<7(−9)	2–6(−9)	0.4—2(−8)	0.3–1(−8)	0.3–1(−8)	1–4(−9)	0.5–2(−8)	0.4–2(−8)	2–6(−9)	0.3–1(−8)
HC_3N	5.71	<1–<0.7(−10)	3–2(−10)	6–4(−10)	7–5(−10)	7–4(−10)	6–4(−10)	9–5(−9)	7–4(−10)	4–3(−10)	4–2(−10)
CH_3SH	···	<1–<7(−9)	<0.4–<3(−9)	<0.5–<3(−9)	0.3–2(−9)	<0.2–<2(−9)	<0.3–<2(−9)	0.4–3(−9)	0.4–3(−9)	<0.3–<2(−9)	<0.4–<3(−9)
H_2CS	5.25	<2–<6(−9)	<0.8–<2(−9)	<0.9–<3(−9)	0.6–2(−9)	0.5–1(−9)	0.5–1(−9)	0.9–3(−9)	0.8–2(−9)	0.8–2(−9)	1–3(−9)
CN	6.24	0.4–2(−8)	0.4–2(−8)	0.4–2(−8)	1–6(−8)	1–6(−8)	2–7(−8)	1–7(−8)	1–5(−8)	0.6–3(−8)	0.5–2(−8)
NS	···	<0.3–<1(−8)	<1–<4(−9)	<1–<4(−9)	1–5(−9)	1–5(−9)	2–5(−9)	2–6(−9)	0.8–3(−9)	<1–<3(−9)	<1–<4(−9)
$C^{17}O$	3.28	<0.6–<3(−7)	<0.2–<1(−7)	0.3–2(−7)	0.4–2(−7)	0.4–2(−7)	0.4–2(−7)	0.4–2(−7)	0.4–2(−7)	0.4–2(−7)	0.3–2(−7)
$N(H_2)$	···	3.6(22)	9.6(22)	7.8(22)	1.6(23)	1.8(23)	1.7(23)	1.6(23)	1.4(23)	1.1(23)	9.6(22)

Notes.

[a] Entries have the form: $a(b) = a \times 10^b$. Molecular hydrogen column densities are determined from the CO(1–0) intensity assuming a conversion factor of $X_{CO} = 0.5 \times 10^{20}$ cm^{-2} (K km s^{-1})$^{-1}$ (Bolatto et al. 2013a). Calculation of the column densities of individual species are calculated assuming LTE excitation. The range quoted for each entry corresponds to 10–75 K. Overall systematic uncertainties, including the adopted excitation temperature (range shown), galactic position (positions 1–3 and 7–10 likely have excitation temperatures at the low end of the range), and the CO conversion factor (uncertain to a factor of three; Bolatto et al. 2013b), dominate the error budget, so separate error bars are not presented for each position. Upper limits are 5σ.

[b] The critical density (not including radiative trapping effects), $\log(n_{cr} = A_{ij}/C_{ij}[100K])$. Rates are adapted from the Leiden LAMDA database, van der Tak et al. 2007, with C_{ij}: HCN/$H^{13}N$/$HN^{13}C$: Dumouchel et al.(2010); HCO^+/$H^{13}CO^+$: Flower (1999); SiO: Dayou & Balança (2006); C_2H: Spielfiedel et al.(2012); HNCO: Green (1986); CS: Lique et al.(2006a); SO: Lique et al.(2006b); HC_3N Green & Chapman (1978); H_2CS: Wiesenfeld & Faure (2013); CN: Lique et al.(2010); $C^{17}O$: Yang et al.(2010).

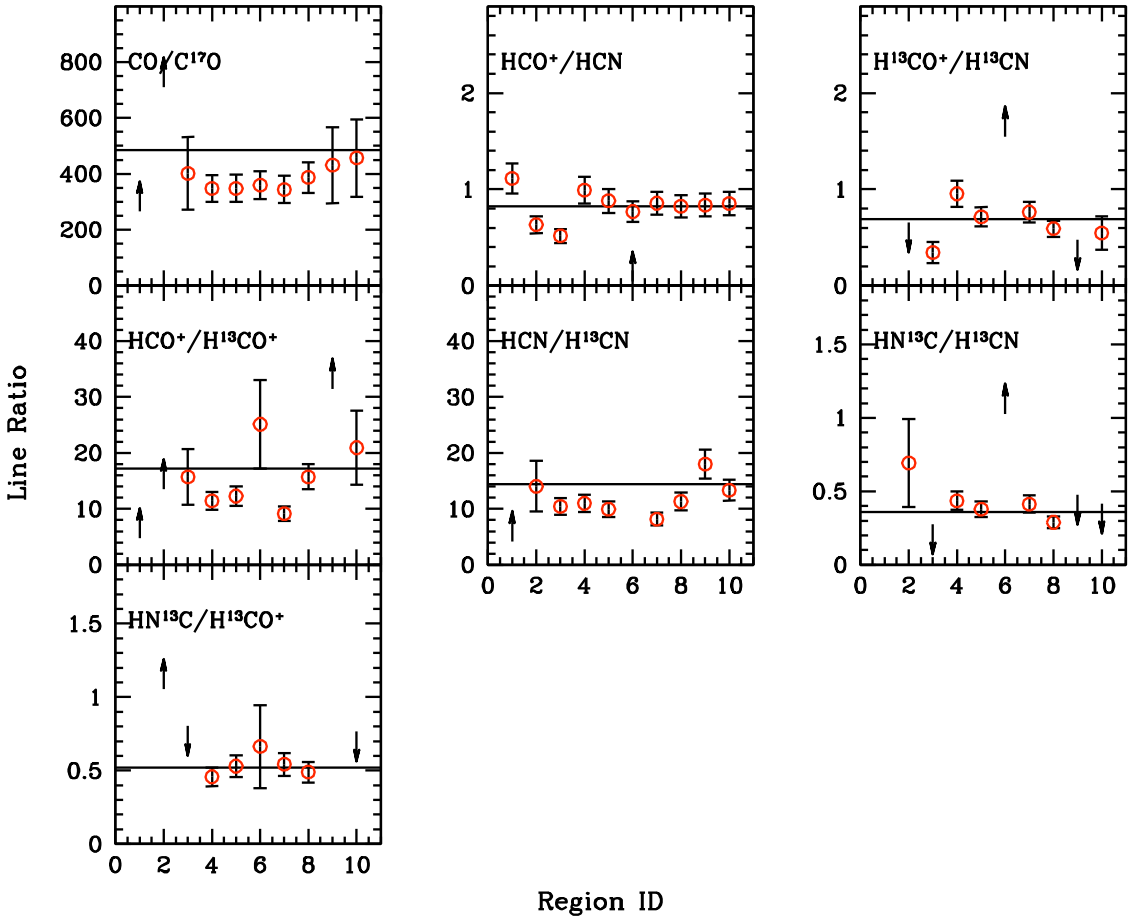

Figure 5. CO and dense gas line ratios (Sections 4.1 and 4.2). The respective line ratio is given in each panel. The x–axis number corresponds to the region number as defined in Section 3.2 and Figure 4. The horizontal line in each panel shows the value for the entire galaxy (i.e., the global ratio). Uncertainties are determined from Table 3.

abundances $[CO/^{13}CO] \gtrsim 60$ (Martín et al. 2010), CO opacities estimated from the $CO/C^{13}O$ line ratios are ∼5 (e.g., Paglione et al. 2004; Sakamoto et al. 2011). This scenario is consistent with $CO/C^{17}O$ data (and $CO/C^{18}O$) if non-LTE effects are at most a factor of ∼2. We conclude that, despite the large column density toward NGC 253's nucleus, CO(1–0) is only modestly opaque. It is likely that this low optical depth is due to increased line widths due to turbulence, the molecular outflow, non-circular motions and/or elevated gas temperatures that reduce the CO opacity per unit velocity.

The moderate CO optical depth is also reflected in the implied sub-Galactic CO-to-H_2 conversion factor in starbursts like NGC 253 (Harrison et al. 1999; Downes & Solomon 1998; Meier & Turner 2001; Bolatto et al. 2013b). A comparison of the LTE $C^{17}O$ column to the H_2 column estimated by an X_{CO} of 0.5×10^{20} cm^{-2} (K km s^{-1})$^{-1}$, gives a value for $[C^{17}O/H_2]$ constant (to within 20 %) of 1.9×10^{-7} across positions 3–10 (using Equation (1) and $T_{ex} = 75$ K, Section 3.4). If $[CO/C^{17}O] = 1000$ and $[CO/H_2] = 10^{-4}$, then we would expect a value of $[C^{17}O/H_2] \simeq 10^{-7}$. The level of agreement between the two methods of constraining $N(H_2)$ is reasonable, being less than the uncertainties in each method. The small differences are an indicator of the uncertainty in $N(H_2)$. Agreement could be made exact by raising $[C^{17}O/H_2]$ and/or by lowering the adopted T_{ex}.

4.2. Dense Gas Tracers and their Isotopologues

The commonly observed dense gas line ratios, HCO^+/HCN, HNC/HCN, and HCO^+/HNC ratios are predicted to be sensitive to gas density, cosmic ray ionization and possibly the X-ray versus UV ionization rate or the present of mechanical heating (e.g., Kohno et al. 2001; Meijerink & Spaans 2005; Graciá-Carpio et al. 2006; Knudsen et al. 2007; Papadopoulos 2007; Krips et al. 2008; Baan et al. 2008; Loenen et al. 2008; Meijerink et al. 2011; Kazandjian et al. 2012). HCO^+(1–0) effective critical densities are nearly a factor of five lower than HCN, so to first order, elevated HCO^+/HCN and HCO^+/HNC ratios are expected in moderate density gas ($n_{H_2} \sim 10^{4.5}$ cm^{-3}). As densities increase, both transitions thermalize and the ratio tends to unity. Moreover, HNC/HCN ratios are expected to drop in energetic environments because HNC is preferential destroyed in hot gas (e.g., Schilke et al. 1992; Meier & Turner 2005). If these transitions have high optical depths, which is probable given the large columns of dense gas, all ratios are driven toward unity. As a result of the large inferred optical depths, changes in these main isotopic line ratios due to interesting physical/chemical changes will be partially hidden.

Here we focus on the dense gas properties in the central starburst region of NGC 253. The HCO^+/HCN intensity ratio (Figure 5) is observed to be slightly less than unity and exhibits very little change over the inner disk (except for position 2 and 3). This suggests that both HCN(1–0) and HCO^+(1–0) are optically thick and slightly subthermal across much of the nucleus (Knudsen et al. 2007). Here we add new HCN/$H^{13}CN$, $HCO^+/H^{13}CO^+$, $H^{13}CO^+/H^{13}CN$, and $HN^{13}C/H^{13}CN$ intensity ratios to further constrain dense gas properties. The isotopologues of HCN, HCO^+, and HNC have lower optical

depths and allow estimates of the line opacity and changes in the abundance ratio of these species.

The observed HCN/$H^{13}CN$ and $HCO^+/H^{13}CO^+$ both have values of 10–15 over much of the inner nuclear disk (Figure 5). The fact that these ratios are much lower than the expected [$^{12}C/^{13}C$] ratio of $\gtrsim$60 (Martín et al. 2010) clearly demonstrates that both HCN(1–0) and HCO^+(1–0) have opacities greater than one. This confirms the conclusions of earlier work (Knudsen et al. 2007). For $A = {}^{12}C/{}^{13}C$ abundance ratios of 80 above and LTE assumptions, both HCN and HCO^+ have $\tau \simeq 5$–8. Interestingly this is an optical depth similar or slightly larger than inferred for CO(1–0) from $C^{17}O$. This is expected because the HCN/$H^{13}CN$ and $HCO^+/H^{13}CO^+$ ratios are quite similar to the observed CO/^{13}CO line ratios (e.g., Paglione et al. 2004; Sakamoto et al. 2011). Such optical depths for HCN and HCO^+ are large. For a $T_{ex} = 75$ K, inferred optically thin HCN abundances are $\sim 2.5 \times 10^{-8}$ (Table 4). However, if the isotopologues of HCN, HCO^+ and HNC have a lower excitation temperature than the main species (likely true, see below), then LTE inferred opacities are lower limits.

The $H^{13}CO^+/H^{13}CN$ ratio in particular shows larger variation (Figure 5) than seen in the main isotopic ratios. Moreover the average values of the ratios are different. Toward the two main inner disk GMCs (positions 5 and 7) HCO^+/HCN and $H^{13}CO^+/H^{13}CN$ have very similar ratios, but toward the outer nuclear disk the isotopic dense gas ratios decrease relative to their main versions. Likewise the average $HN^{13}C/H^{13}CN$ ratio of $\sim$0.35 is significantly lower than the single-dish value for the main species ratio ($\sim$0.74; Baan et al. 2008). The fact that the isotopologue substituted species have ratios farther from unity is consistent with the expectation that high optical depth in the main lines artificially drives the ratio closer to unity. These isotopologue ratios tend to move NGC 253 further into the PDR-like ratio parameter space of Baan et al. (2008), consistent with dense gas abundance ratios influenced by warm, PDR across the inner nuclear disk.

Given the lower opacities of the isotopologues of HCN, HCO^+, and HNC, it is expected that subthermal excitation will be the most relevant non-LTE consideration, therefore it is worth modeling the physical conditions implied by these lines. Knudsen et al. (2007) have modeled the main isotopologues, including selected ΔJ transitions. Here we carry out an independent large velocity gradient (LVG) radiative transfer modeling focusing on the isotopic line ratios. Line ratios are modeled as they are to first order independent of the unknown areal filling factor, and therefore constrain the parameter space more precisely. The model used is patterned after the models of Meier et al. (2008), with J_{max} extended to 20 and collisional coefficients adapted from the Leiden LAMDA database (van der Tak et al. 2007; see Table 4 for references to the individual molecular rate coefficients). To model the radiative transfer, assumptions must be made about the abundance per velocity gradient. Models with a wide range of abundance per velocity gradient ($10^{-11.33}$–$10^{-7.67}$ km^{-1} s pc) were calculated. In general it is not easy to obtain agreement for the line ratios of HCN/HCO^+, HCN/$H^{13}CN$, $HCO^+/H^{13}CO^+$, $H^{13}CO^+/H^{13}CN$, $HN^{13}C/H^{13}CO^+$, and $HN^{13}C/H^{13}CN$. HCO^+'s effective critical density is significantly lower than HCN and so HCO^+ abundances have to be low compared to HCN to obtain ratios of HCO^+/HCN lower than unity. However, pushing HCO^+ abundances too low causes disagreement with the isotopic ratios. If we focus only on the five isotopic line ratios, then reasonable solutions that match all are found over a fairly narrow range of parameter space. We adopt $X_{HCN}/dv/dr = 10^{-8.1}$ km^{-1} s pc and $X_{HCO+}/dv/dr = X_{HNC}/dv/dr = 10^{-8.85}$ km^{-1} s pc, consistent with $X_{HCN} \simeq 2.3 \times 10^{-8}$, $X_{HCO+} \simeq X_{HNC} \simeq 4.2 \times 10^{-9}$, and a velocity gradient of $\sim$3 km s^{-1} pc^{-1}. For the isotopologues, a $^{12}C/^{13}C$ ratio of 80 is adopted. These values are in reasonable agreement with the values listed in Table 4 and the observed gas kinematics. There is room to adjust the abundances per velocity gradient of the five species individually, but keeping HCO^+ and HNC abundances equal does an acceptable job. The low abundance of HCO^+ demanded relative to HCN is a direct consequence of its lower effective critical density.

Figure 6 displays the acceptable parameter space for the ratios observed toward the inner nuclear disk (average of the ratios toward positions 5 and 7) displayed in Figure 5. When admitting uncertainties, good agreement to all five ratios is obtained for $n_{H_2} = 10^{4.5-5.0}$ cm^{-3} and $T_{kin} = 60$–120 K. The cross in Figure 6 marks the location of a representative good fit to all lines. Its values are $n_{H_2} = 10^{4.75}$ cm^{-3} and $T_{kin} = 80$ K. T_{kin} below 60 K challenges the observed ratios for $H^{13}CO^+/H^{13}CN$ and $HN^{13}C/H^{13}CN$, and $T_{kin} > 120$ K begins to disagree with $HCO^+/H^{13}CO^+$. Strictly speaking the HCO^+/HCN ratio is not matched, however the disagreement is small ($\sim$30%), and at the level that we expect other complications such as line width variation and transition depend filling factors to become important. The degree of internal consistency obtained in these simple uniform physical condition models is encouraging.

The favored densities and kinetic temperatures of the dense gas isotopologues match well those previously found in Knudsen et al. (2007), with a range overlapping but favoring about 0.25 dex lower densities. These results confirm Knudsen et al. (2007)'s conclusions that HCN, HNC and (to a somewhat lesser degree) HCO^+ are moderately subthermally excited. The dense gas isotopologues are even more strongly subthermal. For the above favored model, we obtain $T_{ex} = 34$ K and 44 K for HCN and HCO^+, respectively. Corresponding opacities are 13 and 2.4 for HCN and HCO^+. For the isotopologues, T_{ex} [τ] are 7.2 K [2.4], 16 K [0.27], and 5.3 K [0.71] for $H^{13}CN$, $H^{13}CO^+$, and $HN^{13}C$, respectively. LVG modeling demonstrates that while the main transition line opacities crudely match those predicted from LTE, the isotopologue opacities are significantly larger than $^{12}\tau/A$. This stems from the fact that the effective critical density of a transition is dependent on its opacity (radiative trapping), so the isotopologues are more strongly subthermal. As a result, the level populations of the isotopologues settle into the lowest J transitions more efficiently, raising their opacity. This explains the well known effect that isotopic line ratios are gas density probes (e.g., Meier et al. 2000). Furthermore this is strong evidence that the main species, particularly of HCN, must have opacities well in excess of unity.

The slightly larger HCN/$H^{13}CN$ and $HCO^+/H^{13}CO^+$ ratios together with somewhat lower $HN^{13}C/H^{13}CN$ ratios toward the outer nuclear disk are consistent with warm gas that is $\sim$0.5 dex lower in density. However, the decrease in the $H^{13}CO^+/H^{13}CN$ ratio toward the outer disk is somewhat unexpected as gas density is decreasing in this region. Raising T_{kin} significantly will lower the $H^{13}CO^+/H^{13}CN$ ratio slightly even at lower density but only by $\sim$10% for T_{kin} up 300 K. This effect does not appear to be strong enough to explain the observed ratio, and so this ratio is evidence for a small, but genuine abundance enhancement of HCN and its isotopologue relative to HCO^+ and HNC across the nuclear disk—or conversely a decrease of both the isotopologues of HCO^+ and HNC relative to $H^{13}CN$. Invoking mechanical heating may be a viable candidate for

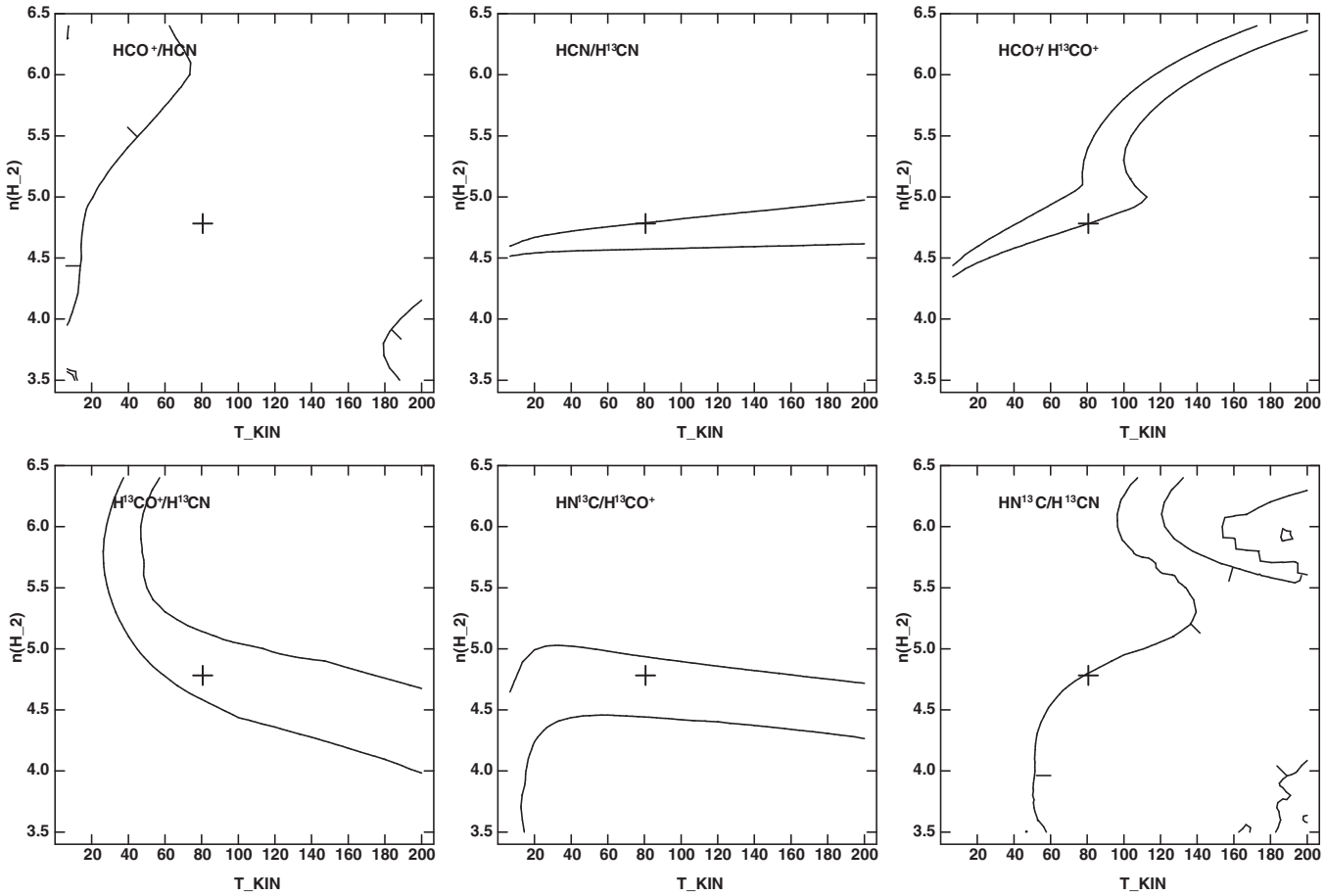

Figure 6. LVG modeling of the inner nuclear disk. The acceptable model predicted parameter space for (clockwise) HCN/HCO^+ $HCN/H^{13}CN$, $HCO^+/H^{13}CO^+$, $H^{13}CO^+/H^{13}CN$, $HN^{13}C/H^{13}CO^+$, and $HN^{13}C/H^{13}CN$1–0 transitions. Contours are the $\pm 1\sigma$ observed line ratio for the average of position 5 and 7. Tick marks indicate the direction of the favored parameter space if it is not obvious. Adopted abundance per velocity gradient values from the six different species are discussed in Section 4.2. The cross marks an example set of parameters ($T_{\rm kin} = 80$ K, $n_{\rm H_2} = 10^{4.75}$ cm^{-3}) that is within 1σ of with all five isotopic ratios. The HCN/HCO^+ line ratio is not matched, but is within 30% of the predicted ratio.

elevating HCN at the expense of HCO^+ and HNC (Loenen et al. 2008; Meijerink et al. 2011; Rosenberg et al. 2014), because hotter gas converts HNC to HCN (e.g., Schilke et al 1992). If mechanical heating is more pronounced at the base of the outflow in the outer disk then this may explain the further drop in $H^{13}CO^+/H^{13}CN$ here. However this possibility is speculative so we consider the explanation for the lower $H^{13}CO^+/H^{13}CN$ ratio unsettled.

4.3. PDR Tracers

Given the strong radiation field in NGC 253's center, the presence of PDR tracers are expected and observed. PDRs warm gas and maintain significant amounts of carbon in ionized form (e.g., Tielens & Hollenbach 1985), so tracers include species that form rapidly from C^+ and H or H_2. These include simple hydrocarbons, such as CH, C_2H, c-C_3H_2, and molecules that form directly from these species, like CN (e.g., Fuente et al. 1993; Sternberg & Dalgarno 1995; Röllig et al. 2007). In molecular gas strongly irradiated by UV photons we expect such species to exhibit elevated abundances. The two main PDR tracers in our data set are CN and C_2H. C_2H has a critical density that is significantly lower than CN (see Table 4), and therefore traces somewhat more diffuse PDRs.

Both CN and C_2H exhibit fine/hyperfine structure splitting and so their opacity can be determined directly. For C_2H the theoretical LTE $C_2H(3/2–1/2)/C_2H(1/2–1/2)$ ratio should be 2.3 in the optically thin limit (for the subset of blended lines included), dropping to 1 when optically thick. We observe a global ratio of ~2.4 (Figure 7). Likewise for CN, the CN(3/2–1/2)/CN(1/2–1/2) fine structure ratio is 2 (Figure 7), which is what we observe for the inner nuclear disk of NGC 253. Both CN and C_2H are likely optically thin and therefore their intensities are proportional to their column densities.

The maps of these two species are strongly dominated by the innermost disk locations, 4–7, where star formation is most intense and where the ionized/molecular outflow originates. Figure 7 displays both the CN(1–0; 3/2–1/2)/CO(1–0) (hereafter CN/CO) and the C_2H(1–0;3/2–1/2)/HCN(1–0) (hereafter C_2H/HCN) line ratios.[10] Both ratios decrease significantly from the inner ($CN/CO \simeq 0.11$; $C_2H/HCN \simeq 0.45$) to the outer ($CN/CO \simeq 0.035$; $C_2H/HCN \simeq 0.18$) nuclear disk. This behavior is explained by a combination of an increased PDR fraction and differential optical depth. To separate these effects, ratios were calculated between optically thin proxies for CO and HCN, $CN/C^{17}O$ and $C_2H/H^{13}CN$ (Figure 7). In both cases the trend for enhanced PDR tracers in the inner disk is seen, though less pronounced. The average $CN/C^{17}O$ ratio is $\lesssim$20 in the outer

[10] These two ratios are chosen instead of the more common ratio, CN/HCN (e.g., Boger & Sternberg 2005), because only they can be obtained from matched array configurations in our data set.

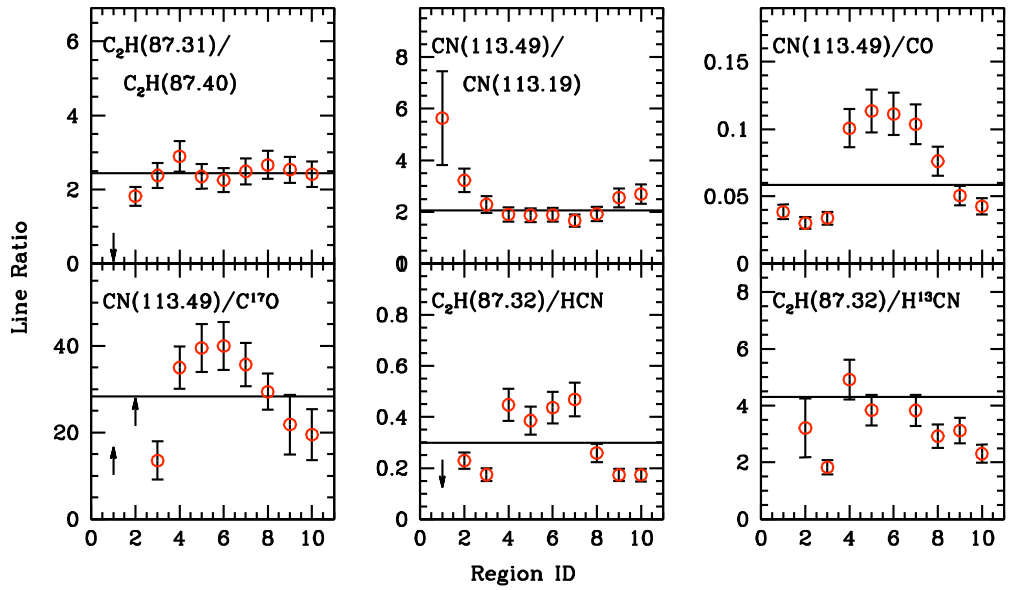

Figure 7. Same as Figure 5, but for PDR tracer line ratios (Section 4.3).

disk and a factor of ∼2 higher toward the inner disk region). Likewise, for $C_2H/H^{13}CN$, the outer disk average is ∼2 and the inner disk average is 3.5–4.5. The fact that $C_2H/H^{13}CN$ and $CN/C^{17}O$ both show the same magnitude of an effect suggests that density changes across the nucleus are not controlling the line ratio. Hence it appears that PDRs constitute a larger fraction of the dense gas toward the inner nuclear disk. Simple hydrocarbons exhibit elevated abundances in this environment. We note that the more complex hydrocarbon symmetric top, CH_3C_2H, has a rather similar morphology to CN and C_2H, suggesting that its abundance can also be elevated in PDRs.

We also note that the PDR tracers are observed in the base of the molecular outflow. This is consistent with the recent detection of C_2H in the molecular outflow in the nucleus of Maffei 2 (Meier & Turner 2012).

4.4. Shock Tracers

Given the intense star forming environment in NGC 253's center and its associated outflow of molecular gas (B13), we expect the presence of shocked gas tracers. Our data set includes two common extragalactic shock tracers, SiO (e.g., García-Burillo et al. 2000) and HNCO (Meier & Turner 2005). HNCO is thought to come from dust ice mantle sublimation (where due to filling factor reasons ice mantle evaporation in hot cores is invisible on larger scales), while SiO is enhanced by ejection of significant Si from sputtered silicate grain cores in high velocity shocks (e.g., Meier & Turner 2005; Rodríguez-Fernández et al. 2010; Tideswell et al. 2010; Martin-Pintado et al. 1992).

SiO emission is distributed across the nucleus in a series of compact sources with some relative enhancement seen toward the eastern outer nuclear disk. Calculated SiO abundances ($X(SiO) \sim 10^{-9}$) confirm that SiO is elevated across the entire nuclear disk. This SiO value is comparable to that seen locally on GMC scales in "shock regions" in other nearby spiral galaxies (e.g., Usero et al. 2006; Meier & Turner 2012) and slightly larger than found in previous NGC 253 SiO measurements (differences are due to different adopted T_{ex} and $N(H_2)$ values; García-Burillo et al. 2000). These abundances are much larger than observed toward quiescent Galactic molecular clouds ($\lesssim 10^{-11}$; e.g., Ziurys et al. 1989; Martin-Pintado et al. 1992).

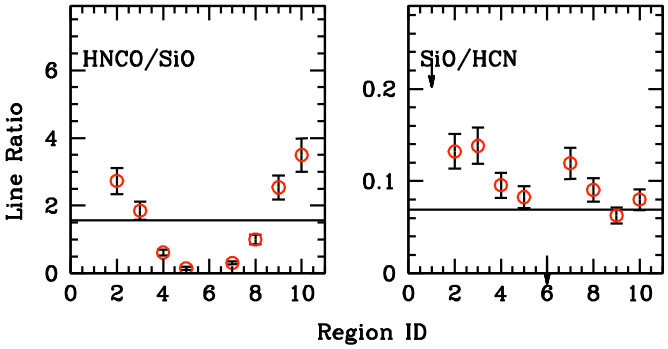

Figure 8. Same as Figure 5, but for shock tracer ratios (Section 4.4).

Interestingly, HNCO has the most distinctive morphology of all the bright lines, being completely dominated by the outer locations of the disk. Such an enhancement at the outer edges of the nuclear disk is also seen in several other nearby barred nuclei, IC 342, Maffei 2, and NGC 6946 (Meier & Turner 2005; 2012). Estimated HNCO abundances reach $\sim 10^{-8}$ across the outer nuclear disk and decrease to $\sim 10^{-9}$ toward the inner nuclear disk. HNCO abundance in quiescent Galactic clouds approach this inner disk value (e.g., Marcelino et al. 2009; Tideswell et al. 2010).

Assuming SiO traces shocks, then the SiO/HCN line ratio can be considered to first order an indicator of the fraction of the dense gas that is experiencing strong shocks. HNCO/SiO ratio is often considered a tracer of shock strength, because the shocks need to be stronger to elevate the SiO abundance (e.g., Usero et al. 2006). In Figure 8 we present these two ratios across the nuclear disk of NGC 253. The SiO/HCN intensity ratio is fairly flat across the disk with slight elevations seen toward regions 2 and 3. This indicates that shocks are uniformly present over much of the nuclear disk in NGC 253. The HNCO/SiO ratio in the outer nuclear disk matches the ratio observed in bar shock regions of nearby spirals like IC 342 (Meier & Turner 2005; Usero et al. 2006) and Maffei 2 (Meier & Turner 2012) well. Toward the inner disk the ratio drops dramatically to a value of ∼0.17. Only M 82 has a ratio anywhere near this low (García-Burillo et al. 2000; Martín et al. 2009a).

At face value this extremely low HNCO/SiO ratio in the inner disk could be taken to indicate that shock strengths decrease away from the core. However, the SiO morphology and abundance suggests that, even in the outer disk, shock strengths are strong enough to keep SiO high relative to HCN. Therefore other effects that further alter the HNCO morphology besides simple shock strength must be considered. Two important second order effects that can alter the HNCO/SiO ratio (see Meier & Turner 2012 for a thorough discussion): (1) HNCO has a significantly higher photodissociation rate than SiO, so its shock signatures are erased more easily in the presence of PDRs/UV radiation fields. (2) SiO is a linear top molecule so its partition function is $\propto T_{\rm ex}$, while HNCO is an asymmetric top molecule, with a partition function $\propto T_{\rm ex}^{1.5}$. So in hot gas, HNCO's lower energy states depopulate more rapidly than SiO. For HNCO this effect is mitigated at $T_{\rm ex} \sim$ 5–20 K by the fact that E_u(HNCO) is $\sim$ 11 K compared to SiO's value of 6.3 K, but if $T_{\rm ex} \sim$ 75 K in the inner disk then this could be a pronounced effect.

In the inner nuclear disk, the gas is hot and PDR dominated (see Section 4.3), so we expect that both act to drive down the HNCO/SiO ratio in the center. Therefore it appears we are observing the starburst (and outflow) actively in the process of erasing the signatures grain mantles species in the inner disk (Martín et al. 2009a, 2009b). In this context it is not surprising that its HNCO/SiO ratio is similar to M 82's, a nucleus where PDRs have completed the task of erasing the weak shock tracers (Takano et al. 1995; García-Burillo et al. 2000).

4.5. Sulfur Species

We detect a significant number of sulfureted species, including CS, SO, NS, H_2CS, CH_3SH, and C_2S. When accounting for the different array configurations used to observe them, CS, SO, H_2CS and NS all have quite similar morphologies. They tend to be dominated by the dense GMCs, with a preference toward the clouds on the northeast side of the continuum peak (7 and 8), whereas the PDR/hydrocarbons tend to favor the southwestern side of the inner disk (position 5). Interestingly, the morphology of the sulfureted species, particularly CS and SO are very similar to SiO. Assuming SiO traces shocked gas (Section 4.4), this hints at a possible connection between the S species and shocked gas. This is somewhat unexpected, at least for CS, given that in other nearby nuclei it has been argued that CS is primarily a PDR tracer (e.g., Meier & Turner 2005; Martín et al. 2009a). Evidently a mix of shocks and strong radiation fields are capable of maintaining high abundances of SiO and CS, though not HNCO.

The CS/SO abundance ratio is sensitive to the C^+/O abundance ratio and it has been argued to be either a tracer of the C/O abundance ratio ($\sim$ 0.4 in the Galaxy), or early versus late time chemistry (e.g., Heithausen et al. 1998; Nilsson et al. 2000). So when C or C^+ is nearly as abundant as atomic O, CS is strongly favored over SO. Our observed SO/CS intensity ratio is $\sim$0.1–0.18 over much of the nuclear disk (Figure 9). This corresponds to a CS/SO abundance ratio of $>$1.5–3 (higher if CS is optically thick), in good agreement with Galactic star forming regions. Nilsson et al. (2000) find values ranging between 0.4–5, with most at $\sim$2.

Likewise, the NS/SO (and NS/CS) abundance ratios are particularly sensitive to atomic C and O abundances. NS is formed from the neutral-neutral reactions, S + NH $\rightarrow$ NS + H and N + SH $\rightarrow$ NS + H. Atomic O destroys both NS and its parent SH, converting them to NO and SO, respectively. Likewise, reactions with C/C^+ drive NS into CS and CN. In star forming regions the radiation field can keep a significant amount of C and O in non-molecular form. As such, standard gas-phase models predict NS cannot not attain abundances above X(NS) $\sim 10^{-11}$ (e.g., McGonagle & Irvine 1997; McElroy et al. 2013). In the inner nuclear disk we observe NS abundances in the range of 1–6$\times 10^{-9}$, at least two orders of magnitude larger than the maximum gas-phase models can accommodate. NS/SO abundances ratios are also high, reaching 0.2–0.5 (the exact values are uncertain due to non-matched array configurations). These elevated abundances are consistent with that determined from single-dish measurements toward NGC 253 (Martín et al. 2003, 2005), except the present observations further demonstrate that the high abundances are attained toward the same inner disk GMCs where PDR conditions are pronounced.

To explain the similar (high) abundances of CS, SO and NS toward the same region requires non-standard chemistry. The atomic abundances of species like O must be kept very low, despite the PDR conditions. Two possible scenarios appear feasible. The first, introduced by Viti et al. (2001) (see also Charnley 1997; Harada et al. 2010 and Izumi et al. 2013), invokes a high temperature gas phase chemistry due to the passage of a shock. This high temperature gas drives O into the more inert H_2O form so it does not destroy NS as rapidly. A second possibility is that in the pre-starburst phase of NGC 253's nucleus, much of the atomic species condensed onto the dust grains where they are converted into their saturated form (e.g., Brown et al. 1988). At a later time shocks liberated the saturated species (e.g., CH_4, NH_3, H_2O, and possibly H_2S). The gas-phase chemistry then evolved from molecular initial conditions, keeping atomic C and O low. Both of the scenarios invoke the presence of shocks, and so are consistent with the tight morphological connection between the sulfur species and SiO.

We observe both ortho-H_2CS at 101 GHz and a mix of para transitions at 103 GHz. The ortho-to-para ratio of H_2CS, the sulfur analog to formaldehyde H_2CO, is useful for constraining the formation conditions of H_2CS (Minh et al. 1991). Under optically thin, high-T ($>$15 K in the case of H_2CS), LTE case, the ratio of the ortho species of H_2CS (those with K_a [K_{-1}] even, see Table 1) to the para (those with K_a odd) should be 3.0. If the temperature at the time of formation is $\leqslant$15 K then the two forms of H_2CS with not be thermalized to their statistical weights and hence have an abundance ratio less than 3—approaching unity at $T = 0$ K. The intensity ratio of the two types of transitions (Figure 9) is approximately constant across the disk at a value of $\sim$1.4. For $T_{\rm ex} = 75$ K the measured ratio implies an ortho-to-para ratio of 2.9. Therefore every position is consistent with standard LTE, high temperature limit. Thus, at least in the case of H_2CS, this suggests that H_2CS formed in the high temperature gas phase after evaporation, or if it was formed on the grain surfaces in an earlier epoch, those surfaces were still significantly warmer than 15 K.

4.6. Millimeter Recombination Lines

We have detected three hydrogen recombination lines in our observations (H40α, H50β, and H52β). The morphology of these recombination lines is very different from all the molecular gas tracers (e.g., Figures 1 and 3): The emission is centrally concentrated, coincident with the location of the underlying continuum emission (L14). Hβ radio recombination lines are reported outside the Local Group for the first time here. The error bars are significant for the β lines, but the global

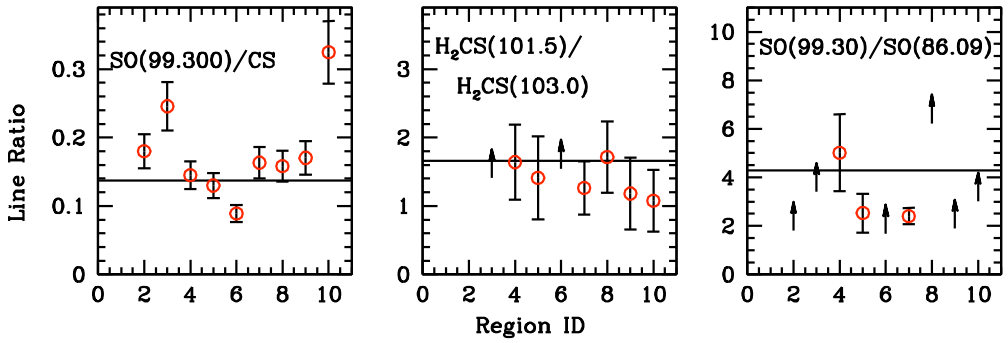

Figure 9. Same as Figure 5, but for sulfur species line ratios (Section 4.5).

H40α/H50β ratio is around 3.5, in good agreement with the LTE value of 3.5 (=1/0.285) for $n_e = 10^4$ cm^{-3} and $T_e = 10^4$ K. The γ lines would be fainter than the β line by a factor of 2.3. Indeed, we do not clearly detect any γ lines. We also do not detect any Heα lines. Other radio/mm recombination lines mapped in NGC 253 have been discussed extensively elsewhere (e.g., Anantharamaiah & Goss 1996; Mohan et al. 2002, 2005; Rodríguez-Rico et al. 2006; Kepley et al. 2011). The morphology of both the α and β lines mapped here are in excellent agreement with the ones reported previously.

4.7. Tentatively Identified Species

We here briefly comment on other selected species detected in our observations.

A large number of tentatively identified lines can be attributed to carbon-rich complex species (e.g., CH_3CH_2CN, CH_3CH_2OH, CH_2CN, CH_2CO, CH_3CHO, and NH_2CHO (Table 1). These species represent the next step in complexity beyond the molecules detected in external galaxies up until now, and suggest that these molecules may be fairly extended in NGC 253.

One unidentified feature detected is of particular interest. This is the feature U-114.22 at ~114.218 GHz. This spectral feature is within <4 MHz (<11 km s^{-1}) of both C_4H(N = 12–11; J = 23/2–21/2; F = 12–11) and the $v = 1$ transition of CO(1–0). The upper energy state of the CO(1–0; $v = 1$) line is 3089 K above ground, so the excitation temperature of the gas must be >450 K in order to explain the observed line ratio. The morphology of this transition is very similar to the radio recombination lines (accounting for resolution differences), as would be expected if it is tracing molecular gas not associated with the cold molecular phase. The C_4H transition has a much lower upper energy level of 35.6 K, typical of the other transitions seen here. Moreover, it is plausible to expect that the C_4H might trace PDR emission (like C_2H), which are also concentrated toward the inner disk, though why it would be significantly more compact than C_2H is unexplained. We consider C_4H as the most likely identification, however the observed morphology indicates that the possibility this feature could be vibrationally excited CO deserves further investigation.

5. SUMMARY AND CONCLUSIONS

We present the detection of a total of 50 molecular lines in the nearby starburst galaxy NGC 253, based on early science (cycle 0) observations taken with the ALMA. For 27 lines we have an unambiguous identification, and 13 lines have tentative IDs (no plausible line identification was possible in 10 cases).

We here describe a schematic picture of the central starburst region of NGC 253 mapped by ALMA (Figure 10): As described in Section 3.1, the nucleus of NGC 253 is characterized by the inner portion of NGC 253's large-scale bar. The outer part of the nuclear disk (the "outer nuclear disk"), likely represents the location where the gas is flowing radially inward along the large-scale bar. Inside this is a compact region exhibiting a large quantity of high density gas and intense star formation, as evidenced by the presence of dense gas (Section 4.2), PDR (Section 4.3) and shock tracers (Section 4.4). This component (the 'inner nuclear disk"), dominates the morphology of most of the spectral lines detected by the observations. We detect high density molecular gas tracers (HCN, HCO^+, and CN) at the base of the molecular outflow first detected in the ^{12}CO emission (B13).

In detail, we find moderate ^{12}CO opacities of ~2–5, despite the large column density toward NGC 253's nucleus. This may be due to increased line–widths due to turbulence, non-circular motions and/or elevated gas temperatures that reduce the CO opacity per unit velocity. Comparing HCN(1–0) and HCO^+(1–0) with their ^{13}C–substituted isotopologues yields that the HCN(1–0) and HCO^+(1–0) are also optically thick, with similar (moderate) opacities to CO. These high HCN and HCO^+ opacities imply that the main isotopologue HCN/HCO^+ (and HCN/HNC) line ratios have less diagnostic power in this starburst environment. Using the isotopically substituted versions of these high density tracers we measure much more robust values for the popular "HCO^+/HCN," "HNC/HCN", and "HNC/HCO^+" ratios. All five of the isotopic dense gas tracer ratios can be well fit by LVG models with $n_{H_2} = 10^{4.75}$ cm^{-3}, $T_{kin} = 80$ K, and X(HCN) ~ 5X(HCO^+) ~ 5X(HNC).

The weak shock tracer/ice mantle species HNCO has the most distinctive morphology of all the bright lines being completely dominated by the outer locations of the disk. This is at odds with what is seen in the strong shock tracer, SiO. Attributing the dramatic variation in the HNCO and SiO maps across the nucleus to changing shock strength is unsatisfactory because SiO is enhanced across the nucleus at a level that should imply shocks are strong throughout the inner disk. A possible explanation for the faintness of HNCO is that because of its higher photodissociation rate relative to SiO, the ice mantle evaporation shock signatures are being preferentially erased in the presence of the intense central radiation fields. This is consistent with the presence of an enhanced PDR fraction toward the region of HNCO's dramatic decrease as determined form the CN/C^{17}O and C_2H/H^{13}CN ratios. The sulfureted species appear also to be (indirectly) connected to the presence of shocks across the inner disk.

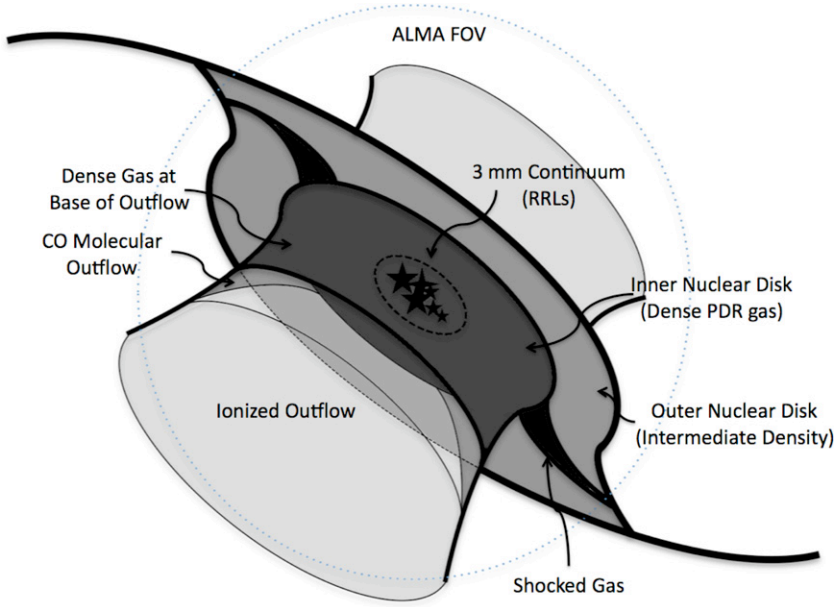

Figure 10. Schematic picture of the central starburst region of NGC 253 (see discussion in Section 5). The morphology is based on Figure 1 of B13 with the chemistry added.

We have detected three hydrogen recombination lines (H40α, H50β and H52β) that show a centrally concentrated morphology (similar to the underlying continuum emission) that is distinctly different from all molecular gas tracers.

Finally, we report some tentative identifications, including the aldehydes CH_3CHO and NH_2CHO, cyanides CH_2CN and CH_3CH_2CN, and a number of organics of similar complexity, CH_2CO, HCOOH, and CH_3CH_2OH. The first vibrational state of the ^{12}CO(1–0) line is also possibly detected. If follow-up, multi-line studies confirm these IDs then they would represent the first extragalactic detections of the above species.

D.S.M. acknowledges partial support by the National Science Foundation through grant AST-1009620. A.D.B. acknowledges support by the Alexander von Humboldt Foundation and the Federal Ministry for Education and Research through a Humboldt Fellowship, support by the National Science Foundation through CAREER grant AST-0955836 and AST-1412419, as well as a Cottrell Scholar award from the Research Corporation for Science Advancement. We thank the anonymous referee for a thorough and helpful review. This paper makes use of the following ALMA data: ADS/JAO.ALMA #2011.0.00172.S. ALMA is a partnership of ESO (representing its member states), NSF (USA), and NINS (Japan), together with NRC (Canada), and NSC and ASIAA (Taiwan), in cooperation with the Republic of Chile. The Joint ALMA Observatory is operated by ESO, AUI/NRAO and NAOJ. The National Radio Astronomy Observatory is a facility of the National Science Foundation operated under cooperative agreement by Associated Universities, Inc.

Facility: ALMA

REFERENCES

Aladro, R., Martín-Pintado, J., Martín, S., Mauersberger, R., & Bayet, E. 2011, A&A, 525, A89
Aladro, R., Viti, S., Bayet, E., et al. 2013, A&A, 549, AA39
Anantharamaiah, K. R., & Goss, W. M. 1996, ApJL, 466, L13
Baan, W. A., Henkel, C., Loenen, A. F., Baudry, A., & Wiklind, T. 2008, A&A, 477, 747
Boger, G. I., & Sternberg, A. 2005, ApJ, 632, 302
Bolatto, A. D., Warren, S. R., Leroy, A. K., et al. 2013a, Natur, 499, 450 (B13)
Bolatto, A. D., Wolfire, M., & Leroy, A. K. 2013b, ARA&A, 51, 207
Brown, P. D., Charnley, S. B., & Millar, T. J. 1988, MNRAS, 231, 409
Carilli, C. L., & Walter, F. 2013, ARA&A, 51, 105
Charnley, S. B. 1997, ApJ, 481, 396
Costagliola, F., Aalto, S., Rodriguez, M. I., et al. 2011, A&A, 528, A30
Cummins, S. E., Linke, R. A., & Thaddeus, P. 1986, ApJS, 60, 819
Dayou, F., & Balança, C. 2006, A&A, 459, 297
Downes, D., & Solomon, P. M. 1998, ApJ, 507, 615
Dumouchel, F., Faure, A., & Lique, F. 2010, MNRAS, 406, 2488
Flower, D. R. 1999, MNRAS, 305, 651
Fuente, A., Martin-Pintado, J., Cernicharo, J., & Bachiller, R. 1993, A&A, 276, 473
García-Burillo, S., Martín-Pintado, J., Fuente, A., & Neri, R. 2000, A&A, 355, 499
Graciá-Carpio, J., García-Burillo, S., Planesas, P., & Colina, L. 2006, ApJL, 640, L135
Green, S. 1986, NASA Tech. Memo., NASA TM 87791
Green, S., & Chapman, S. 1978, ApJS, 37, 169
Harada, N., Herbst, E., & Wakelam, V. 2010, ApJ, 721, 1570
Harrison, A., Henkel, C., & Russell, A. 1999, MNRAS, 303, 157
Heithausen, A., Corneliussen, U., & Grossmann, V. 1998, A&A, 330, 311
Henkel, C., Asiri, H., Ao, Y., et al. 2014, A&A, 565, AA3
Houghton, S., Whiteoak, J. B., Koribalski, B., et al. 1997, A&A, 325, 923
Hunter, S. D., Bertsch, D. L., Catelli, J. R., et al. 1997, ApJ, 481, 205
Izumi, T., Kohno, K., Martín, S., et al. 2013, PASJ, 65, 100
Kazandjian, M. V., Meijerink, R., Pelupessy, I., Israel, F. P., & Spaans, M. 2012, A&A, 542, AA65
Kennicutt, R. C., & Evans, N. J. 2012, ARA&A, 50, 531
Kepley, A. A., Chomiuk, L., Johnson, K. E., et al. 2011, ApJL, 739, L24
Knudsen, K. K., Walter, F., Weiss, A., et al. 2007, ApJ, 666, 156
Kohno, K., Matsushita, S., Vila-Vilaró, B., et al. 2001, in ASP Conf. Ser. 249, The Central Kiloparsec of Starbursts and AGN: The La Palma Connection, ed. J. H. Knapen, J. E. Beckman, I. Shlosman, & T. J. Mahoney (San Francisco, CA: ASP), 672
Krips, M., Neri, R., García-Burillo, S., et al. 2008, ApJ, 677, 262
Ladd, E. F. 2004, ApJ, 610, 320
Leroy, A. K., Bolatto, A., Ostriker, E. C., et al. 2014, ApJ, in press (arXiv:1411.2836) (L14)
Lique, F., Spielfiedel, A., & Cernicharo, J. 2006a, A&A, 451, 1125
Lique, F., Spielfiedel, A., Dhont, G., & Feautrier, N. 2006b, A&A, 458, 331
Lique, F., Spielfiedel, A., Feautrier, N., et al. 2010, JChPh, 132, 024303
Loenen, A. F., Spaans, M., Baan, W. A., & Meijerink, R. 2008, A&A, 488, L5
Marcelino, N., Cernicharo, J., Tercero, B., & Roueff, E. 2009, ApJL, 690, L27
Martín, S., Aladro, R., Martín-Pintado, J., & Mauersberger, R. 2010, A&A, 522, A62
Martín, S., Kohno, K., Izumi, T., et al. 2015, A&A, 573, A116

Martín, S., Martín-Pintado, J., & Mauersberger, R. 2009a, ApJ, 694, 610
Martín, S., Martín-Pintado, J., Mauersberger, R., Henkel, C., & García-Burillo, S. 2005, ApJ, 620, 210
Martín, S., Martín-Pintado, J., & Viti, S. 2009b, ApJ, 706, 1323
Martín, S., Mauersberger, R., Martín-Pintado, J., García-Burillo, S., & Henkel, C. 2003, A&A, 411, L465
Martín, S., Mauersberger, R., Martín-Pintado, J., Henkel, C., & García-Burillo, S. 2006, ApJS, 164, 450
Martin-Pintado, J., Bachiller, R., & Fuente, A. 1992, A&A, 254, 315
McElroy, D., Walsh, C., Markwick, A. J., et al. 2013, A&A, 550, A36
McGonagle, D., & Irvine, W. M. 1997, ApJ, 477, 711
Meier, D. S., & Turner, J. L. 2001, ApJ, 551, 687
Meier, D. S., & Turner, J. L. 2005, ApJ, 618, 259
Meier, D. S., & Turner, J. L. 2012, ApJ, 755, 104
Meier, D. S., Turner, J. L., & Beck, S. C. 2014, ApJ, 795, 107
Meier, D. S., Turner, J. L., & Hurt, R. L. 2000, ApJ, 531, 200
Meier, D. S., Turner, J. L., & Hurt, R. L. 2008, ApJ, 675, 281
Meijerink, R., & Spaans, M. 2005, A&A, 436, 397
Meijerink, R., Spaans, M., Loenen, A. F., & van der Werf, P. P. 2011, A&A, 525, AA119
Minh, Y. C., Irvine, W. M., & Brewer, M. K. 1991, A&A, 244, 181
Mohan, N. R., Anantharamaiah, K. R., & Goss, W. M. 2002, ApJ, 574, 701
Mohan, N. R., Goss, W. M., & Anantharamaiah, K. R. 2005, A&A, 432, 1
Nakajima, T., Takano, S., Kohno, K., & Inoue, H. 2011, ApJL, 728, LL38
Nguyen-Q-Rieu , Henkel, C., Jackson, J. M., & Mauersberger, R. 1991, A&A, 241, L33
Nilsson, A., Hjalmarson, Å., Bergman, P., & Millar, T. J. 2000, A&A, 358, 257
Ott, J., Weiss, A., Henkel, C., & Walter, F. 2005, ApJ, 629, 767
Paglione, T. A. D., Tosaki, T., & Jackson, J. M. 1995, ApJL, 454, L117
Paglione, T. A. D., Wall, W. F., Young, J. S., et al. 2001, ApJS, 135, 183
Paglione, T. A. D., Yam, O., Tosaki, T., & Jackson, J. M. 2004, ApJ, 611, 835
Papadopoulos, P. P. 2007, ApJ, 656, 792
Rekola, R., Richer, M. G., McCall, M. L., et al. 2005, MNRAS, 361, 330
Rodríguez-Fernández, N. J., Tafalla, M., Gueth, F., & Bachiller, R. 2010, A&A, 516, A98
Rodríguez-Rico, C. A., Goss, W. M., Zhao, J.-H., Gómez, Y., & Anantharamaiah, K. R. 2006, ApJ, 644, 914
Röllig, M., Abel, N. P., Bell, T., et al. 2007, A&A, 467, 187
Rosenberg, M. J. F., Kazandjian, M. V., van der Werf, P. P., et al. 2014, A&A, 564, AA126
Sakamoto, K., Mao, R.-Q., Matsushita, S., et al. 2011, ApJ, 735, 19
Schilke, P., Walmsley, C. M., Pineau Des Forets, G., et al. 1992, A&A, 256, 595
Snell, R. L., Narayanan, G., Yun, M. S., et al. 2011, AJ, 141, 38
Spielfiedel, A., Feautrier, N., Najar, F., et al. 2012, MNRAS, 421, 1891
Sternberg, A., & Dalgarno, A. 1995, ApJS, 99, 565
Strong, A. W., Bloemen, J. B. G. M., Dame, T. M., et al. 1988, A&A, 207, 1
Takano, S., Nakai, N., & Kawaguchi, K. 1995, PASJ, 47, 801
Tideswell, D. M., Fuller, G. A., Millar, T. J., & Markwick, A. J. 2010, A&A, 510, AA85
Tielens, A. G. G. M., & Hollenbach, D. 1985, ApJ, 291, 722
Turner, B. E. 1991, ApJS, 76, 617
Usero, A., García-Burillo, S., Fuente, A., Martín-Pintado, J., & Rodríguez-Fernández, N. J. 2004, A&A, 419, 897
Usero, A., García-Burillo, S., Martín-Pintado, J., Fuente, A., & Neri, R. 2006, A&A, 448, 457
van der Tak, F. F. S., Black, J. H., Schöier, F. L., Jansen, D. J., & van Dishoeck, E. F. 2007, A&A, 468, 627
Viti, S., Caselli, P., Hartquist, T. W., & Williams, D. A. 2001, A&A, 370, 1017
Wiesenfeld, L., & Faure, A. 2013, MNRAS, 432, 2573
Wilson, T. L., & Rood, R. 1994, ARA&A, 32, 191
Wouterloot, J. G. A., Henkel, C., Brand, J., & Davis, G. R. 2008, A&A, 487, 237
Yang, B., Stancil, P. C., Balakrishnan, N., & Forrey, R. C. 2010, ApJ, 718, 1062
Ziurys, L. M., Friberg, P., & Irvine, W. M. 1989, ApJ, 343, 201